

MOLECULAR SCALE CONTACT LINE HYDRODYNAMICS OF IMMISCIBLE FLOWS

Tiezheng Qian

*Department of Physics and Institute of Nano Science and Technology,
The Hong Kong University of Science and Technology,
Clear Water Bay, Kowloon, Hong Kong, China*

Xiao-Ping Wang

*Department of Mathematics,
The Hong Kong University of Science and Technology,
Clear Water Bay, Kowloon, Hong Kong, China*

Ping Sheng*

*Department of Physics and Institute of Nano Science and Technology,
The Hong Kong University of Science and Technology,
Clear Water Bay, Kowloon, Hong Kong, China*

Abstract

From extensive molecular dynamics simulations on immiscible two-phase flows, we find the relative slipping between the fluids and the solid wall everywhere to follow the generalized Navier boundary condition, in which the amount of slipping is proportional to the sum of tangential viscous stress and the uncompensated Young stress. The latter arises from the deviation

*To whom correspondence should be addressed. E-mail: sheng@ust.hk

of the fluid-fluid interface from its static configuration. We give a continuum formulation of the immiscible flow hydrodynamics, comprising the generalized Navier boundary condition, the Navier-Stokes equation, and the Cahn-Hilliard interfacial free energy. Our hydrodynamic model yields interfacial and velocity profiles matching those from the molecular dynamics simulations at the molecular-scale vicinity of the contact line. In particular, the behavior at high capillary numbers, leading to the breakup of the fluid-fluid interface, is accurately predicted.

47.11.+j, 68.08.-p, 83.10.Mj, 83.10.Ff, 83.50.Lh

I. INTRODUCTION

Immiscible two-phase flow in the vicinity of the contact line (CL), where the fluid-fluid interface intersects the solid wall, is a classical problem that falls beyond the framework of conventional hydrodynamics [1–12]. In particular, molecular dynamics (MD) studies have shown relative slipping between the fluids and the wall, in violation of the no-slip boundary condition [6,7]. There have been numerous ad-hoc models [1,8,10–12] to address this phenomenon, but none was able to give a quantitative account of the MD slip velocity profile in the molecular-scale vicinity of the CL. While away from the moving CL the small amount of relative slipping was found to follow the Navier boundary condition (NBC) [13], i.e., relative slipping proportional to the tangential viscous stress, in the molecular-scale vicinity of the CL the NBC failed totally to account for the near-complete slip. This failure casts doubts on the general applicability of the NBC to immiscible flows and hinders a continuum formulation of the hydrodynamics in the CL region. In particular, a (possible) breakdown in the hydrodynamic description for the molecular-scale CL region has been suggested [7]. Without a continuum hydrodynamic formulation, it becomes difficult or impossible to have realistic simulations of micro- or nanofluidics, or of immiscible flows in porous media where the relative wetting characteristics, the moving CL dissipation, and behavior over undulating solid surfaces may have macroscopic implications.

From MD simulations on immiscible two-phase flows, we report the finding that the generalized Navier boundary condition (GNBC) applies for all boundary regions, whereby the relative slipping is proportional to the sum of tangential viscous stress and the uncompensated Young stress. The latter arises from the deviation of the fluid-fluid interface from its static configuration [10]. By combining GNBC with the Cahn-Hilliard (CH) hydrodynamic formulation of two-phase flow [11,12], we obtained a consistent, continuum description of immiscible flow with predictions matching those from MD simulations. Our findings suggest the no-slip boundary condition to be an approximation to the GNBC, accurate for most macroscopic flows but failing in immiscible flows.

II. MOLECULAR DYNAMICS SIMULATIONS

The MD simulations were performed for both the static and dynamic configurations in Couette and Poiseuille flows. The two immiscible fluids were confined between two parallel walls separated along the z direction, with the fluid-solid boundaries defined by $z = 0, H$ (see Fig. 1 for Couette geometry). Interaction between the fluid molecules was modeled by a modified Lennard-Jones (LJ) potential $U_{ff} = 4\epsilon [(\sigma/r)^{12} - \delta_{ff}(\sigma/r)^6]$, where r is the distance between the molecules, ϵ and σ are the energy scale and range of interaction, respectively, and $\delta_{ff} = 1$ for like molecules and $\delta_{ff} = -1$ for molecules of different species. Each of the two walls was constructed by two (or more) [001] planes of an fcc lattice (see Appendix A), with each wall molecule attached to the lattice site by a harmonic spring. The mean-squared displacement of wall molecules was controlled to obey the Lindemann criterion. The wall-fluid interaction was also modeled by a LJ potential U_{wf} , with energy and range parameters $\epsilon_{wf} = 1.16\epsilon$ and $\sigma_{wf} = 1.04\sigma$, and a δ_{wf} for specifying the wetting property of the fluid. Both U_{ff} and U_{wf} were cut off at $r_c = 2.5\sigma$. The mass of the wall molecule was set equal to that of the fluid molecule m , and the average number densities for the fluids and wall were set at $\rho = 0.81/\sigma^3$ and $\rho_w = 1.86/\sigma^3$, respectively. The temperature was controlled at $2.8\epsilon/k_B$, where k_B is Boltzmann's constant. Moving the top and bottom walls at a constant speed V in the $\pm x$ directions, respectively, induced the Couette flow [7]. Applying a body force $m\mathbf{g}_{ext}$ to each fluid molecule in the x direction induced the Poiseuille flow [6]. Periodic boundary conditions were imposed on the x and y boundaries of the sample. Most of our MD simulations were carried out on samples consisting 6144 atoms for each fluid and 2880 atoms for each wall. The sample is 163.5σ by 6.8σ along the x and y , respectively, and $H = 13.6\sigma$. Our MD results represent time averages over 20 to 40 million time steps. For technical details of our MD simulations, we followed those described in Ref. [14].

Two different cases were considered in our simulations. The symmetric case refers to identical wall-fluid interactions for the two fluids (both $\delta_{wf} = 1$), which leads to a flat static

interface in the yz plane with a 90° contact angle. The asymmetric case refers to different wall-fluid interactions, with $\delta_{wf} = 1$ for one and $\delta_{wf} = 0.7$ for the other. The resulting static interface is a circular arc with a 64° contact angle. We measured six quantities in the Couette-flow steady states of $V = 0.25(\epsilon/m)^{1/2}$, $H = 13.6\sigma$ for the symmetric case and $V = 0.2(\epsilon/m)^{1/2}$, $H = 13.6\sigma$ for the asymmetric case: v_x^{slip} , the slip velocity relative to the moving wall; G_x^w , the tangential force per unit area exerted by the wall; the σ_{xx} , σ_{nx} components of the fluid stress tensor (n denotes the outward surface normal), and v_x , v_z .

We denote the region within $0.85\sigma = z_0$ of the wall the boundary layer (BL). It must be thin enough to render sufficient precision for measuring v_x^{slip} , while thick enough to fully account for the tangential wall-fluid interaction force, due to the finite range of the LJ interaction. Thus it is not possible to do MD measurements strictly at the fluid-solid boundary, not only because of poor statistics, but also because of this intrinsic limitation. The wall force can be identified by separating the force on each fluid molecule into wall-fluid and fluid-fluid components. For $0 < z \leq z_0$ the fluid molecules can detect the atomic structure of the wall. When coupled with kinetic collisions with the wall molecules, there arises a nonzero tangential wall force that varies along the z direction and saturates at $z \simeq z_0$. G_x^w is the saturated total tangential wall force per unit wall area (Fig. 2). In Appendix A we give account of our MD results on both the tangential and normal components of the wall force, plus the effect(s) of increasing the wall thickness in our simulations from 2 layers of wall molecules to 4 layers and to infinite layers (by using the continuum approximation beyond the 4 layers).

Spatial resolution along the x and z directions was achieved by evenly dividing the sampling region into bins, each $\Delta x = 0.425\sigma$ by $\Delta z = 0.85\sigma$ in size. v_x^{slip} was obtained as the time average of fluid molecules' velocities inside the BL, measured with respect to the moving wall; G_x^w was obtained from the time average of the total tangential wall force experienced by the fluid molecules in the BL, divided by the bin area in the xy plane; $\sigma_{xx(nx)}$ was obtained from the time averages of the kinetic momentum transfer plus the fluid-fluid interaction forces across the constant- $x(z)$ bin surfaces, and $v_{x(z)}$ was measured as the time-averaged

velocity component(s) within each bin. For the contribution of intermolecular forces to the stress, we have directly measured the fluid-fluid interaction forces across bin surfaces instead of using the Irving-Kirkwood expression [15], whose validity was noted to be not justified at the fluid-fluid or the wall-fluid interface (see the paragraph following equation (5.15) in the above reference). In Appendix B we give some details on our MD stress measurements. As reference quantities, we also measured G_x^{w0} , σ_{xx}^0 , σ_{nx}^0 in the static ($V = 0$) configuration. In addition, we measured in both the static and dynamic configurations the average molecular densities ρ_1 and ρ_2 for the two fluid species in each bin to determine the interface profile. The shear viscosity $\eta = 1.95\sqrt{\epsilon m}/\sigma^2$ and the interfacial tension $\gamma = 5.5\epsilon/\sigma^2$ were also determined.

We have also measured the interface and velocity profiles for the Poiseuille flow in the asymmetric case, as well as for Couette flows with different V and H in the symmetric case.

III. GENERALIZED NAVIER BOUNDARY CONDITION

We present evidences to show that everywhere on the boundaries, relative slipping is proportional to the net tangential force per unit area exerted on the three (fluid) sides of the BL fluid element, due to the hydrodynamic motion of the surrounding fluid(s) (the GNBC, see also equation (3) below):

$$\tilde{G}_x^f = \beta v_x^{slip}, \quad (1)$$

where β is the slip coefficient, over tilde denotes the quantity to be the difference between the dynamic and static values (e.g., $\tilde{\sigma}_{xx(nx)} = \sigma_{xx(nx)} - \sigma_{xx(nx)}^0$), and \tilde{G}_x^f denotes

$$\tilde{G}_x^f = \partial_x \int_0^{z_0} dz \tilde{\sigma}_{xx}(z) - \tilde{\sigma}_{nx}(z_0), \quad (2)$$

obtained by integrating from 0 to z_0 the x -direction hydrodynamic force density, $\partial_x \tilde{\sigma}_{xx} + \partial_z \tilde{\sigma}_{zx}$, minus the tangential stress $\tilde{\sigma}_{nx}(0)$ at the fluid-solid boundary. Here the z coordinate is for the lower fluid-solid boundary (same below), with the understanding that the same

physics holds at the upper boundary, and $\partial_{x,z,n}$ means taking partial derivative with respect to x , z , or surface normal n ($\partial_n = -\partial_z$ for the lower boundary). We have verified the steady state force balance $\tilde{G}_x^w + \tilde{G}_x^f = 0$ on the two boundaries (inset to Fig. 3) [16]. In Fig. 3 we show the measured MD data for the symmetric and asymmetric cases in the Couette geometry. The symbols represent the values of \tilde{G}_x^f measured in the BL. The solid lines represent the values of \tilde{G}_x^f calculated from βv_x^{slip} by using $\beta = \beta_1 = \beta_2 = 1.2\sqrt{\epsilon m}/\sigma^3$ for the symmetric case and $\beta_1 = 1.2\sqrt{\epsilon m}/\sigma^3$, $\beta_2 = 0.532\sqrt{\epsilon m}/\sigma^3$ for the asymmetric case away from the CL region (straight line segments in Fig. 3), and $\beta = (\beta_1\rho_1 + \beta_2\rho_2)/(\rho_1 + \rho_2)$ in the CL region [17], with v_x^{slip} and $\rho_{1,2}$ obtained from MD simulations. It is seen that for the lower boundary (upper right panel), the MD data agree well with the predictions of Eq. (1). For the upper boundary (lower left panel) the straight line segments also agree well with Eq. (1). However, there is some discrepancy in the interfacial region of the upper boundary that seems to arise from a “shear thinning” effect of decreasing β at very large tangential stresses [13].

The fact that the wall force density is distributed inside a thin BL and vanishes beyond the BL necessitates the form of \tilde{G}_x^f as defined by Eq. (2). However, it is intuitively obvious that the fluids would experience almost the identical physical effect(s) from a wall force density $\tilde{G}_x^w\delta(z)$, concentrated strictly at the fluid-solid boundary with the same total wall force per unit area. The replacement of a diffuse boundary by a sharp boundary can considerably simplify the form of the GNBC, because local force balance along x then requires $\partial_x\tilde{\sigma}_{xx} + \partial_z\tilde{\sigma}_{zx} = 0$ in the fluid. Integration of this relation from 0 to z_0 yields $\tilde{G}_x^f = -\tilde{\sigma}_{nx}(0)$ (by comparing with Eq. (2)). Thus the GNBC (1) becomes $-\tilde{\sigma}_{nx}(0) = \beta v_x^{slip}$ in the sharp boundary limit.

The tangential stress $\tilde{\sigma}_{nx}$ can be decomposed into a viscous component and a non-viscous component: $\tilde{\sigma}_{nx}(z) = \sigma_{nx}^v(z) + \tilde{\sigma}_{nx}^Y(z)$. In Fig. 4 we show that away from the interfacial region the tangential viscous stress $\sigma_{nx}^v(z) = \eta(\partial_n v_x + \partial_x v_n)(z)$ is the only nonzero component, but in the interfacial region $\tilde{\sigma}_{nx}^Y = \sigma_{nx} - \sigma_{nx}^v - \sigma_{nx}^0 = \sigma_{nx}^Y - \sigma_{nx}^0$ is dominant, thereby accounting for the failure of NBC to describe the CL motion. Therefore away from the CL region the NBC is

valid, but in the interfacial region the NBC clearly fails to describe the CL motion. We wish to clarify the origin of σ_{nx}^Y and σ_{nx}^0 as the dynamic and static Young stresses, respectively, so that $\tilde{\sigma}_{nx}^Y = \sigma_{nx}^Y - \sigma_{nx}^0$ is the uncompensated Young stress. As shown in the inset to Fig. 4, the integrals (across the interface) of σ_{nx}^Y ($= \sigma_{nx} - \sigma_{nx}^v$, calculated by subtracting the viscous component $\eta(\partial_n v_x + \partial_x v_n)$ from the total tangential stress σ_{nx}) and σ_{nx}^0 are equal to $\gamma \cos \theta_d$ and $\gamma \cos \theta_s$, respectively, at different values of z , i.e., $-\int_{\text{int}} dx \sigma_{nx}^Y(z) = \gamma \cos \theta_d(z)$ and $-\int_{\text{int}} dx \sigma_{nx}^0(z) = \gamma \cos \theta_s(z)$, where $\theta_d(z)$ and $\theta_s(z)$ are respectively the dynamic and static interfacial angles at z [18]. These results clearly show the origin of the extra tangential stress in the interfacial region to be the interfacial (uncompensated) Young stress. Thus the GNBC is given by

$$\beta v_x^{\text{slip}} = -\tilde{\sigma}_{nx}(0) = -[\eta \partial_n v_x](0) - \tilde{\sigma}_{nx}^Y(0). \quad (3)$$

Here only one component of the viscous stress is nonzero, due to $v_n = 0$ at the boundary; and $-\tilde{\sigma}_{nx}^Y(0)$ is denoted the uncompensated Young stress, satisfying $-\int_{\text{int}} \tilde{\sigma}_{nx}^Y(0) dx = \gamma(\cos \theta_d^0 - \cos \theta_s^0)$, with $\theta_{d(s)}^0$ being a microscopic dynamic (static) contact angle at the fluid-solid boundary. The fact that $\tilde{\sigma}_{nx}^Y(0) \approx 0$ away from the CL shows that the GNBC implies NBC for single phase flows.

Due to the diffuse nature of the BL in MD simulations, the contact angle $\theta_{d(s)}^0$ cannot be directly measured. Nevertheless, they are obtainable through extrapolation by using the integrated interfacial curvature within the BL. That is, in the sharp boundary limit the force balance in the fluids is expressed by $\partial_x \tilde{\sigma}_{xx} + \partial_n \tilde{\sigma}_{nx} = 0$. Integration in z across the BL gives

$$\partial_x \int_0^{z_0} dz \tilde{\sigma}_{xx}(z) - \sigma_{nx}^v(z_0) + \sigma_{nx}^v(0) - \tilde{\sigma}_{nx}^Y(z_0) + \tilde{\sigma}_{nx}^Y(0) = 0. \quad (4)$$

Integration (of Eq. (4) along x) across the fluid-fluid interface then yields

$$\Delta \left[\int_0^{z_0} dz \tilde{\sigma}_{xx}(z) \right] - \int_{\text{int}} dx \sigma_{nx}^v(z_0) + \int_{\text{int}} dx \sigma_{nx}^v(0) + \gamma \mathcal{K}_d - \gamma \mathcal{K}_s = 0. \quad (5)$$

where $\Delta [\int_0^{z_0} dz \tilde{\sigma}_{xx}(z)]$ is the change of the z -integrated $\tilde{\sigma}_{xx}$ across the interface, \mathcal{K}_d and \mathcal{K}_s denote the dynamic and static z -integrated interfacial curvatures:

$$\mathcal{K}_d = \cos \theta_d(z_0) - \cos \theta_d^0,$$

and

$$\mathcal{K}_s = \cos \theta_s(z_0) - \cos \theta_s^0.$$

Here $\Delta [\int_0^{z_0} dz \tilde{\sigma}_{xx}(z)]$, $\sigma_{nx}^v(z_0)$, $\theta_d(z_0)$, and $\theta_s(z_0)$ are obtainable from MD simulations, $K_s \simeq \pm 2z_0 \cos \theta_s^0/H$ for the circular static interfaces, while $\sigma_{nx}^v(0) = \eta[\partial_n v_x](0)$ may be obtained by extrapolating from the values of tangential viscous stress at $z = z_0, 2z_0$, and $3z_0$. Therefore the microscopic dynamic contact angle θ_d^0 can be obtained from Eq. (5). We have measured the z -integrated $\tilde{\sigma}_{xx} = \sigma_{xx} - \sigma_{xx}^0$ in the BL. The dominant behavior is a sharp drop across the interface, as shown in Fig. 5 for both the symmetric and asymmetric cases. The value of θ_d^0 obtained is $88 \pm 0.5^\circ$ for the symmetric case and $63 \pm 0.5^\circ$ for the asymmetric case at the lower boundary, and $64.5 \pm 0.5^\circ$ at the upper boundary. These values are noted to be very close to θ_s^0 . Yet the small difference between the dynamic and static (microscopic) contact angles is essential in accounting for the near complete slip in the CL region.

In essence, our results show that in the vicinity of the CL, the tangential viscous stress $-\sigma_{nx}^v$ as postulated by the NBC can not give rise to the near-complete CL slip without taking into account the tangential Young stress $-\sigma_{nx}^Y$ in combination with the gradient of the (BL-integrated) normal stress σ_{xx} . For the static configuration, the normal stress gradient is balanced by the Young stress, leading to the Young equation. It is only for a moving CL that there is a component of the Young stress which is no longer balanced by the normal stress gradient, and this uncompensated Young stress is precisely the additional component captured by the GNBC but missed by the NBC.

IV. CONTINUUM HYDRODYNAMIC FORMULATION

For Eq. (3) to serve as a boundary condition in hydrodynamic calculations, we need to derive the local value of the uncompensated Young stress $\tilde{\sigma}_{nx}^Y(0)$ from a continuum formulation of the immiscible flow hydrodynamics. Such a formulation is important for studying the macroscopic implications of moving CL's under scenarios beyond the capability of MD simulations. As a first-order approximation, we formulate a hydrodynamic model based on

the GNBC and the CH free energy functional [19] that has been successful in the calculations of fluid-fluid interfacial phenomena:

$$F[\phi] = \int d\mathbf{r} \left[\frac{1}{2} K (\nabla\phi)^2 + f(\phi) \right], \quad (6)$$

where $\phi = (\rho_2 - \rho_1)/(\rho_2 + \rho_1)$, $f(\phi) = -\frac{1}{2}r\phi^2 + \frac{1}{4}u\phi^4$, and K, r, u are parameters which can be directly obtained from MD simulations through the interface profile thickness $\xi = \sqrt{K/r}$ [20], the interfacial tension $\gamma = 2\sqrt{2}r^2\xi/3u$, and the two homogeneous equilibrium phases given by the condition of $\partial f/\partial\phi = 0$, yielding $\phi_{\pm} = \pm\sqrt{r/u}$ ($= \pm 1$ in our case).

To derive the effects of the CH free energy F on immiscible flow hydrodynamics, let us consider a composition field $\phi(\mathbf{r})$. A displacement of the molecules from \mathbf{r} to $\mathbf{r}' = \mathbf{r} + \mathbf{u}(\mathbf{r})$ induces a local change of ϕ , $\delta\phi = -\mathbf{u} \cdot \nabla\phi$, to the first order in \mathbf{u} . The associated change in F is given by the sum of a body term and a surface term:

$$\delta F = - \int d\mathbf{r} [\mathbf{g} \cdot \mathbf{u}] + \int ds [\sigma_{ni}^Y u_i], \quad (7)$$

where $\mathbf{g} = \mu\nabla\phi$ is the capillary force density, with $\mu = \delta F/\delta\phi = -K\nabla^2\phi - r\phi + u\phi^3$ being the chemical potential, and

$$\sigma_{ni}^Y = -K\partial_n\phi\partial_i\phi, \quad (8)$$

is the tangential Young stress due to the spatial variation of ϕ at the fluid-solid boundary ($i \perp n$). Hence the two coupled equations of motion are the Navier-Stokes equation (with the addition of the capillary force density) and the convection-diffusion equation for $\phi(\mathbf{r})$:

$$\rho_m \left[\frac{\partial \mathbf{v}}{\partial t} + (\mathbf{v} \cdot \nabla) \mathbf{v} \right] = -\nabla p + \nabla \cdot \boldsymbol{\sigma}^v + \mu\nabla\phi + \rho_m \mathbf{g}_{ext}, \quad (9)$$

$$\frac{\partial \phi}{\partial t} + \mathbf{v} \cdot \nabla\phi = M\nabla^2\mu, \quad (10)$$

together with the incompressibility condition $\nabla \cdot \mathbf{v} = 0$. Here ρ_m is the fluid mass density, p is the pressure, $\boldsymbol{\sigma}^v$ denotes the viscous part of the stress tensor, $\rho_m \mathbf{g}_{ext}$ is the external body force density (for Poiseuille flows), and M is the phenomenological mobility coefficient.

Four boundary conditions are required to solve Eqs. (9) and (10). Two are given by the impermeability condition, i.e., the normal components of the fluid velocity and diffusive flux are zero: $v_n = 0$ and $\partial_n \mu = 0$. The other two boundary conditions may be derived from the total free energy

$$F_{tot}[\phi] = F[\phi] + \int ds \gamma_{wf}(\phi), \quad (11)$$

where $\gamma_{wf}(\phi)$ is the interfacial free energy per unit area at the fluid-solid boundary. We use $\gamma_{wf}(\phi) = (\Delta\gamma_{wf}/2) \sin(\pi\phi/2)$ to denote a smooth interpolation between $\pm\Delta\gamma_{wf}/2$, with $\Delta\gamma_{wf} = \gamma_{wf}(\phi_+) - \gamma_{wf}(\phi_-)$ given by $-\gamma \cos \theta_s^0$ (Young's equation). Here it should be noted that the form of the smooth interpolation has very little effect on the final results. Hence we have chosen a simple interpolation function. Similar to Eq. (7), the change in F_{tot} due to the displacement of the molecules from \mathbf{r} to $\mathbf{r}' = \mathbf{r} + \mathbf{u}(\mathbf{r})$ is given by

$$\delta F_{tot} = - \int d\mathbf{r} [\mathbf{g} \cdot \mathbf{u}] + \int ds [\tilde{\sigma}_{ni}^Y u_i], \quad (12)$$

where

$$\tilde{\sigma}_{ni}^Y = - \left[K \partial_n \phi + \frac{\partial \gamma_{wf}(\phi)}{\partial \phi} \right] \partial_i \phi, \quad (13)$$

is the uncompensated Young stress [12] (see below). The continuum form of the GNBC (3) is therefore given by

$$\beta v_x^{slip} = -\tilde{\sigma}_{nx}(0) = -\eta [\partial_n v_x](0) + [L(\phi) \partial_x \phi](0), \quad (14)$$

where $[L(\phi) \partial_x \phi](0)$, with $L(\phi) = K \partial_n \phi + \partial \gamma_{wf}(\phi)/\partial \phi$, is the differential expression for $-\tilde{\sigma}_{nx}^Y(0) = -\sigma_{nx}^Y(0) + \sigma_{nx}^0(0)$ in equation (3). Here $K \partial_n \phi \partial_x \phi$ is $-\sigma_{nx}^Y(0)$ as seen in Eq. (8), and $[\partial \gamma_{wf}(\phi)/\partial \phi] \partial_x \phi = \partial_x \gamma_{wf}(\phi)$ [21] equals to $\sigma_{nx}^0(0)$, in accordance with the static force balance relation $\partial_x \gamma_{wf}(\phi) - \sigma_{nx}^0(0) = 0$. From $\int_{\text{int}} dx [K \partial_n \phi \partial_x \phi](0) = \gamma \cos \theta_d^0$ [22] and $\int_{\text{int}} dx \partial_x \gamma_{wf} = -\gamma \cos \theta_s^0$, we see that

$$\int_{\text{int}} dx [L(\phi) \partial_x \phi](0) = \gamma (\cos \theta_d^0 - \cos \theta_s^0),$$

in agreement with $[L(\phi)\partial_x\phi](0)$ being the uncompensated Young stress.

Another boundary condition may be inferred from the fact that $L(\phi) = 0$ is the Euler-Lagrange equation at the fluid-solid boundary for minimizing the total free energy $F_{tot}[\phi]$. That is, $L(\phi) = 0$ corresponds with the equilibrium (static) condition where $\partial\phi/\partial t + \mathbf{v} \cdot \nabla\phi = 0$. The boundary relaxation dynamics of ϕ is plausibly assumed to be the first-order extension of that correspondence for a nonzero $L(\phi)$:

$$\frac{\partial\phi}{\partial t} + \mathbf{v} \cdot \nabla\phi = -\Gamma [L(\phi)], \quad (15)$$

where Γ is a (positive) phenomenological parameter.

V. COMPARISON OF MD AND CONTINUUM HYDRODYNAMICS RESULTS

Motivated by the methods presented in [23,24], a second order scheme is designed to solve the CH hydrodynamic model, comprising the dynamic equations and the four boundary conditions. Details of the numerical algorithm are presented in Appendix C. Besides those parameters which can be directly obtained from MD simulations, M and Γ are treated as fitting parameters, determined by comparison with MD results (values given in the caption to Fig. 6). In Figs. 1 and 6 we show that the continuum model can indeed quantitatively reproduce the interface and velocity profiles from MD simulations, including the near-complete slip ($v_x \approx 0$ in Fig. 6) of the CL, the fine features in the molecular-scale vicinity of the CL, and the fast pressure variation in the BL (inset to Fig. 6), with its implied large interfacial curvature. We wish to emphasize that for the comparison with the symmetric case, the parameters in the continuum model, including those in the GNBC, are directly obtained from the MD simulations, whose velocity profiles are then fitted by those from the hydrodynamic calculations with optimized M and Γ values. Thus the comparison with the asymmetric (Couette) case, with β_2 directly evaluated from MD simulation data, is *without adjustable parameters*. We have also obtained $\theta_d^0 = 88.1^\circ$ and 62.8° for the symmetric and asymmetric (the lower boundary) cases shown in Figs. 1a and 1b, respectively. Both are in excellent

agreement with their extrapolated values in MD simulations. For the upper boundary in the asymmetric case, our calculated $\theta_d^0 = 65.2^\circ$, which differs somewhat from the MD extrapolation value of $64.5 \pm 0.5^\circ$. This difference is a reflection of the discrepancy seen in Fig. 3. However, it is noteworthy that the difference in the dynamic contact angles does not show up in the velocity profiles, which agree well.

To further verify that the boundary conditions and the parameter values are local properties and hence applicable to flows with different macroscopic conditions, we have varied the wall speed V , the system size H , and the flow geometry to check that the same set of parameters plus the GNBC are valid for reproducing (a) the velocity profiles from a different set of Couette-flow simulations in the symmetric configurations, shown in Fig. 7, as well as (b) the velocity profiles of the Poiseuille flow simulations in the asymmetric case, shown in Fig. 8. The remarkable overall agreement in all cases affirms the validity of GNBC and the hydrodynamic model [25], as well as justifies the replacement of the diffuse fluid-solid boundary (force density) by a sharp boundary.

Another comparison is the dissipation incurred by the moving CL in the Couette flow geometry. Rate of heat generation per unit wall area is given by $|\tilde{G}_x^w|V = \beta|v_x^{slip}|V$. From this we have to subtract a small but constant relative slipping away from the interface, $v_0^{slip} = 2Vl_s/(H + 2l_s)$, where $l_s = \eta/\beta$ is a slip length for fluid 1 if $\phi < 0$ and for fluid 2 if $\phi > 0$. The resulting heat generation rate due to the CL is $\beta V^2 W_s L$ (for one wall), where L is the length of the CL and W_s defines the width of the CL region:

$$W_s = \frac{1}{V} \int (|v_x^{slip}| - v_0^{slip}) dx. \quad (16)$$

Thus CL dissipation is equivalent to a segment, $\sim H(W_s/l_s)$, of dissipation by single phase flow. Figure 9 shows the variation of W_s as a function of capillary number $Ca = \eta V/\gamma$ for the symmetric case of Couette flow. Close to $Ca \simeq 0.1$ the value of W_s increases rapidly, in good agreement with the MD results, and beyond which the continuum model failed to converge. This corresponds to the breakup of the interface observed in MD simulations [26].

VI. CONCLUDING REMARKS

In summary, we have found for the first time the boundary condition that yields near-complete slipping of the CL, in good agreement with MD results on the molecular scale. These results open the door to efficient simulations of micro- or nanofluidics involving immiscible components, as well as to macroscopic immiscible flow calculations, e.g., in porous media, that are physically meaningful at the molecular level [27]. It should also be noted, however, that the present continuum formulation can not calculate fluctuation effects that are important in MD simulations. Long range interactions, e.g., that due to van der Waals interaction, have also been ignored. The latter is potentially important in the calculations involving wetting layers.

ACKNOWLEDGMENTS

Partial support from HKUST's EHIA funding and Hong Kong RGC grants HKUST 6176/99P and 6143/01P is hereby acknowledged.

APPENDIX A: WALL-FLUID INTERACTIONS

We have measured both the tangential and normal components of the wall force exerted on the fluids. Both components vary along the z direction and saturate somewhere away from the fluid-solid boundary. The tangential component saturates (by 99.8%) at $z = z_0$, which is well inside the wall-fluid interaction range ($z_0 = 0.85\sigma$, smaller than the cut-off distance $r_c = 2.5\sigma$ for the wall-fluid interaction potential U_{wf}). On the other hand, the normal component is 87% of the saturation value at $z = z_0$ and 99.8% at $z = 2z_0$. The different saturation ranges of the tangential and normal components may be understood as follows.

For a fluid molecule close to the solid wall, the interaction with one particular (the closest) wall molecule can be much stronger than all the others. As this fluid molecule

moves laterally but still remaining its close proximity to the wall, it would thus experience a strong periodic modulation in its interaction with the wall. This lateral inhomogeneity is an important source for the tangential component of the wall force. Away from the fluid-solid boundary, each fluid molecule can interact with many wall molecules on a nearly equal basis. Thus the modulation amplitude of the wall potential would clearly decrease with increasing distance from the wall. Hence the tangential wall force tends to saturate at the relatively short range of $z \simeq z_0$. On the contrary, the normal wall force directly arises from the wall-fluid interaction, independent of whether the wall potential is “rough” or not. Consequently, the normal wall force saturates much slower than the tangential component.

The MD results presented in this paper were obtained from simulations using solid walls constructed by two [001] planes of an fcc lattice. We have also carried out MD simulations using thicker confining walls. First we changed the number of molecular layers ([001] planes of fcc lattice) from two to four in constructing each of the two walls. The wall-fluid interaction potential U_{wf} were still cut off at $r_c = 2.5\sigma$. It turned out that neither component of the wall force shows any noticeable change. The reason is that for the tangential component, the two outer planes are too distant to contribute to the roughness of the wall potential, while for the normal component, the fluid molecules closest to the wall are separated from the two outer planes by a distance $\geq r_c$. Consequently, both the interface and velocity profiles do not show any noticeable change.

Additional wall layers do not contribute to the perceived modulation of the wall potential by the fluid molecules. Nevertheless, they can still affect the tangential wall force by modifying the organization of the fluid molecules near the wall. Such organization is governed by the wall-fluid interaction and can be greatly influenced by the normal wall force. To see the effects of normal wall force due to additional wall layers, we used four [001] planes of an fcc lattice plus a half-space continuum in constructing a wall. The first four solid layers show the atomic structure detectable by the fluid molecules while the half-space continuum models the deeper solid layers. The wall-fluid interaction was modelled as follows. For a in-range pair of fluid and wall molecules separated by a distance $r < r_c$, the interaction potential is

still U_{wf} . Here the wall molecule must be from one of the four solid layers. In addition to this short-range interaction, the fluid molecules can also experience the long-range interaction potential due to (1) the distant wall molecules in the four solid layers and (2) the continuum. For (1) we integrated the $1/r^6$ term in U_{wf} over the out-of-range ($r > r_c$) area of the solid layers while for (2) we integrated the same term over the half-space continuum. According to this model, only the in-range ($r < r_c$) part of the solid wall shows atomic structure to a fluid molecule while the out-of-range ($r > r_c$) part is effectively a half-space continuum.

We found that the effect of the long-range normal wall force (for $\delta_{wf} > 0$) is to attract the fluid molecules to the wall. In fact the average number density in the BL can increase by 3 – 4% once the long-range force is included. As a result, the slip coefficient $\beta_{1(2)}$ increases by $\sim 5 - 15\%$. This results in small but visible changes in the interface and velocity profiles.

These tests have convinced us that by using two [001] planes of an fcc lattice to model the solid wall, we have captured the dominant wall-fluid interaction. In fact, using two molecular layers to model the solid wall has been extensively practiced in the past MD simulations [6,7,13,25,28], although in some instances more molecular layers have also been used [29], where the accurate modeling of the normal component of the wall-fluid interaction force is important.

APPENDIX B: STRESS MEASUREMENTS IN MD SIMULATIONS

Irving and Kirkwood [15] have shown that in the hydrodynamic equation of motion (momentum transport), the stress tensor (flux of momentum) may be expressed in terms of molecular variables as

$$\boldsymbol{\sigma}(\mathbf{r}, t) = \boldsymbol{\sigma}_K(\mathbf{r}, t) + \boldsymbol{\sigma}_U(\mathbf{r}, t), \tag{B1}$$

where $\boldsymbol{\sigma}_K$ is the kinetic contribution to the stress tensor, given by

$$\boldsymbol{\sigma}_K(\mathbf{r}, t) = - \left\langle \sum_i m_i \left[\frac{\mathbf{P}_i}{m_i} - \mathbf{V}(\mathbf{r}, t) \right] \left[\frac{\mathbf{P}_i}{m_i} - \mathbf{V}(\mathbf{r}, t) \right] \delta(\mathbf{x}_i - \mathbf{r}), f \right\rangle, \tag{B2}$$

and $\boldsymbol{\sigma}_U$ is the contribution of intermolecular forces to the stress tensor, given by

$$\boldsymbol{\sigma}_U(\mathbf{r}, t) = -\frac{1}{2} \left\langle \sum_i \sum_{j \neq i} (\mathbf{x}_i - \mathbf{x}_j) \mathbf{F}_{ij} \delta(\mathbf{x}_i - \mathbf{r}), f \right\rangle. \quad (\text{B3})$$

Here m_i , \mathbf{p}_i , and \mathbf{x}_i are respectively the mass, momentum, and position of molecule i , $\mathbf{V}(\mathbf{r}, t)$ is the local average velocity, \mathbf{F}_{ij} is the force on molecule i due to molecule j , f is the probability distribution function

$$f(\mathbf{x}_1, \dots, \mathbf{x}_N, \mathbf{p}_1, \dots, \mathbf{p}_N, t),$$

which satisfies the normalization condition

$$\int d\mathbf{x}_1 \dots d\mathbf{x}_N d\mathbf{p}_1 \dots d\mathbf{p}_N f = 1,$$

and the Liouville equation

$$\frac{\partial f}{\partial t} = - \sum_i \left[\frac{\mathbf{p}_i}{m_i} \cdot \frac{\partial f}{\partial \mathbf{x}_i} - \nabla_{\mathbf{x}_i} U \cdot \frac{\partial f}{\partial \mathbf{p}_i} \right],$$

with U being the potential energy of the system, and $\langle \dots, f \rangle$ means taking the average for a probability distribution function f .

Although widely employed in the stress measurements in MD simulations, the above expression for $\boldsymbol{\sigma}_U$ (Eq. (B3)) represents only the leading term in an asymptotic expansion, accurate when the interaction range is small compared to the range of hydrodynamic variation [15]. This can be seen as follows.

Consider that all the molecules interact via a pair potential $U_{\text{pair}}(R)$ such that the intermolecular force $\mathbf{F}_{ij} = (\mathbf{R}/R)U'_{\text{pair}}(R)$ for $\mathbf{x}_j = \mathbf{x}_i + \mathbf{R}$. Accordingly, Eq. (B3) can be rewritten as

$$\boldsymbol{\sigma}_U(\mathbf{r}, t) = \frac{1}{2} \int d\mathbf{R} \frac{\mathbf{R}\mathbf{R}}{R} U'_{\text{pair}}(R) \rho^{(2)}(\mathbf{r}, \mathbf{r} + \mathbf{R}, t), \quad (\text{B4})$$

where $\rho^{(2)}$ is the pair density defined by

$$\rho^{(2)}(\mathbf{r}_1, \mathbf{r}_2, t) = \sum_{i \neq j} \langle \delta(\mathbf{r}_i - \mathbf{r}_1) \delta(\mathbf{r}_j - \mathbf{r}_2), f \rangle.$$

It has been shown (see the appendix in Ref. [15]) that according to the definition that $d\mathbf{S} \cdot \boldsymbol{\sigma}_U$ is the force acting across dS , the full expression for $\boldsymbol{\sigma}_U$ is given by

$$\boldsymbol{\sigma}_U(\mathbf{r}, t) = \frac{1}{2} \int d\mathbf{R} \frac{\mathbf{R}\mathbf{R}}{R} U'_{\text{pair}}(R) \left[\int_0^1 d\alpha \rho^{(2)}(\mathbf{r} - \alpha\mathbf{R}, \mathbf{r} - \alpha\mathbf{R} + \mathbf{R}, t) \right]. \quad (\text{B5})$$

It is readily seen that Eq. (B4) may be obtained from Eq. (B5) by keeping only the lowest order term in a Taylor's series in α , i.e.,

$$\rho^{(2)}(\mathbf{r} - \alpha\mathbf{R}, \mathbf{r} - \alpha\mathbf{R} + \mathbf{R}, t) \approx \rho^{(2)}(\mathbf{r}, \mathbf{r} + \mathbf{R}, t).$$

That means $\mathbf{R} \cdot \nabla_{\mathbf{r}} \rho^{(2)}(\mathbf{r}, \mathbf{r} + \mathbf{R}, t)$ must be negligible compared with $\rho^{(2)}(\mathbf{r}, \mathbf{r} + \mathbf{R}, t)$. Here \mathbf{R} is on the order of the range of intermolecular force. This approximation, however, can not be justified at the fluid-fluid or the wall-fluid interface, where $\mathbf{R} \cdot \nabla_{\mathbf{r}} \rho^{(2)}(\mathbf{r}, \mathbf{r} + \mathbf{R}, t)$ can be comparable in magnitude to $\rho^{(2)}$.

In the study of moving CL, it is of great importance to obtain the correct information about stress distributions at both the fluid-fluid and the wall-fluid interfaces. Therefore, we have directly measured the x component of fluid-fluid interaction forces acting across the $x(z)$ bin surfaces, in order to obtain the $xx(zx)$ component of $\boldsymbol{\sigma}_U$. For example, in measuring σ_{Uzx} at a given z -direction bin surface, we recorded all the pairs of molecules interacting across that surface. Here ‘‘interacting across’’ means that the line connecting a pair of molecules intersects the bin surface. For those pairs, we then computed σ_{Uzx} at the given bin surface using

$$\sigma_{Uzx} = \frac{1}{\delta s_z} \sum_{(i,j)} F_{ijx},$$

where δs_z is the area of z -direction bin surface, (i, j) indicate all possible pairs of molecules interacting across the bin surface, with molecule i being ‘‘inside of $\hat{\mathbf{z}}\delta s_z$ ’’ and molecule j being ‘‘outside of $\hat{\mathbf{z}}\delta s_z$ ’’ (molecule i is below molecule j), and F_{ijx} is the x component of the force on molecule i due to molecule j . A schematic illustration is shown in Fig. 10.

For comparison, we have measured the xx and zx components of $\boldsymbol{\sigma}_U$ using the discrete version of Irving-Kirkwood expression (B3):

$$\boldsymbol{\sigma}_U = -\frac{1}{2\delta v} \left\langle \sum_i \sum_{j \neq i} (\mathbf{x}_i - \mathbf{x}_j) \mathbf{F}_{ij} \right\rangle,$$

where δv is the volume of sampling bin, i runs over fluid molecules in the sampling bin, j runs over fluid molecules in interaction with molecule i , and $\langle \dots \rangle$ means taking the time average.

We found that far from the the fluid-fluid and the wall-fluid interfaces, the results based on the Irving-Kirkwood expression agree well with those from direct force measurement, whereas near the fluid-fluid or the wall-fluid interface, the two results show appreciable differences (up to 50%), especially for the zx component at the fluid-fluid interface.

APPENDIX C: NUMERICAL ALGORITHM

We present our numerical algorithm for solving the continuum hydrodynamic model, comprising the dynamic equations (9) and (10) and the four boundary conditions $v_n = 0$, $\partial_n \mu = 0$, plus Eqs. (14) and (15). We pay special attention to the application of boundary conditions, and restrict our analysis to the Couette flow because the generalization to Poiseuille flow is straightforward.

1. Dimensionless hydrodynamic equations

To obtain a set of dimensionless equations suitable for numerical computations, we scale ϕ by $|\phi_{\pm}| = \sqrt{r/u}$, length by $\xi = \sqrt{K/r}$, velocity by the wall speed V , time by ξ/V , and pressure/stress by $\eta V/\xi$. In dimensionless forms, the convection-diffusion equation reads

$$\frac{\partial \phi}{\partial t} + \mathbf{v} \cdot \nabla \phi = \mathcal{L}_d \nabla^2 (-\nabla^2 \phi - \phi + \phi^3), \quad (\text{C1})$$

the Navier-Stokes equation reads

$$\mathcal{R} \left[\frac{\partial \mathbf{v}}{\partial t} + (\mathbf{v} \cdot \nabla) \mathbf{v} \right] = -\nabla p + \nabla^2 \mathbf{v} + \mathcal{B} (-\nabla^2 \phi - \phi + \phi^3) \nabla \phi, \quad (\text{C2})$$

the relaxation of ϕ at the fluid-solid boundary is governed by

$$\frac{\partial \phi}{\partial t} + v_x \partial_x \phi = -\mathcal{V}_s \left[\partial_n \phi - \frac{\sqrt{2}}{3} \cos \theta_s^0 s_\gamma(\phi) \right], \quad (\text{C3})$$

and the GNBC becomes

$$[\mathcal{L}_s(\phi)]^{-1} v_x^{slip} = \mathcal{B} \left[\partial_n \phi - \frac{\sqrt{2}}{3} \cos \theta_s^0 s_\gamma(\phi) \right] \partial_x \phi - \partial_n v_x. \quad (\text{C4})$$

Here $\beta(\phi) = (1 - \phi)\beta_1/2 + (1 + \phi)\beta_2/2$ and $s_\gamma(\phi) = (\pi/2) \cos(\pi\phi/2)$. Five dimensionless parameters appear in the above equations. They are (1) $\mathcal{L}_d = Mr/V\xi$, which is the ratio of a diffusion length Mr/V to ξ , (2) $\mathcal{R} = \rho V\xi/\eta$, (3) $\mathcal{B} = r^2\xi/u\eta V = 3\gamma/2\sqrt{2}\eta V$, which is inversely proportional to the capillary number $Ca = \eta V/\gamma$, (4) $\mathcal{V}_s = K\Gamma/V$, which is the ratio of $K\Gamma$ (of velocity dimension) to V , and (5) $\mathcal{L}_s(\phi) = \eta/\beta(\phi)\xi$, which is the ratio of the slip length $l_s(\phi) = \eta/\beta(\phi)$ to ξ .

2. Finite-difference scheme

For immiscible Couette flows, there are four variables ϕ , v_x , v_z , and p to be solved in a two-dimensional (2D) system (in the xz plane). We want to solve the convection-diffusion equation and the Navier-Stokes equation in a 2D system of length L_x (along x) and height L_z (along z). Here L_x must be large enough to allow the single phase flows (far from the fluid-fluid interface) to approach uniform shear flows. A finite-difference scheme is employed as follows. (1) N_x and N_z equally spaced levels are introduced in the x and z directions, respectively. Grid size is given by $\Delta_x = L_x/(N_x - 1)$ and $\Delta_z = L_z/(N_z - 1)$ along x and z , respectively. (2) Each variable (q) is defined at $N_x \times N_z$ sites distributed from $x = -L_x/2$ to $L_x/2$ and from $z = -L_z/2$ to $L_z/2$, represented by the array $q_{i,j}$, with $i = 1, \dots, N_x$ and $j = 1, \dots, N_z$. Here $q_{i,j} \equiv q(x_i, z_j)$, with $x_i = (i - 1)L_x/(N_x - 1) - L_x/2$ and $z_j = (j - 1)L_z/(N_z - 1) - L_z/2$. (3) In applying the various boundary conditions, “ghost” sites outside the system, i.e., $i = 0$, $i = N_x + 1$, $j = 0$, or $j = N_z + 1$, may appear in the discretization scheme. The values of the variables at the ghost sites are determined separately from the various boundary conditions, detailed below. (4) First and second spatial derivatives along ζ ($=x$ or z) are represented by $\partial_\zeta q(\zeta_k) = [q(\zeta_{k+1}) - q(\zeta_{k-1})]/2\Delta_\zeta$ and $\partial_\zeta^2 q(\zeta_k) = [q(\zeta_{k+1}) + q(\zeta_{k-1}) - 2q(\zeta_k)]/\Delta_\zeta^2$.

3. Convection-diffusion equation

With the chemical potential $\mu_{i,j}$ given by

$$\mu_{i,j} = - \left[\frac{\phi_{i+1,j} - 2\phi_{i,j} + \phi_{i-1,j}}{\Delta_x^2} + \frac{\phi_{i,j+1} - 2\phi_{i,j} + \phi_{i,j-1}}{\Delta_z^2} \right] - \phi_{i,j} + \phi_{i,j}^3, \quad (\text{C5})$$

the discretized convection-diffusion equation is

$$\frac{\partial}{\partial t} \phi_{i,j} + [\mathbf{v} \cdot \nabla \phi]_{i,j} = \mathcal{L}_d \left[\frac{\mu_{i+1,j} - 2\mu_{i,j} + \mu_{i-1,j}}{\Delta_x^2} + \frac{\mu_{i,j+1} - 2\mu_{i,j} + \mu_{i,j-1}}{\Delta_z^2} \right], \quad (\text{C6})$$

with

$$[\mathbf{v} \cdot \nabla \phi]_{i,j} = v_{xi,j} \frac{\phi_{i+1,j} - \phi_{i-1,j}}{2\Delta_x} + v_{zi,j} \frac{\phi_{i,j+1} - \phi_{i,j-1}}{2\Delta_z}. \quad (\text{C7})$$

The boundary conditions at $x = \pm L_x/2$ can be easily applied using $\phi = \pm 1$ and

$$\mathbf{v}(z) = \frac{L_z}{L_z + 2L_s} \frac{2z}{L_z} \hat{\mathbf{x}}, \quad (\text{C8})$$

for single-phase uniform shear flows. Here we focus on the boundary conditions at $z = \pm L_z/2$: $\partial_n \mu = 0$ and Eq. (C3). We spell out the numerics for the lower boundary $j = 1$, with the understanding that the same can be applied to the upper boundary.

To solve the discretized convection-diffusion equation (C6) at the lower boundary $j = 1$, we need the values of $\mu_{i,j}$ at $j = 1$ and $j = 0$. We also need the values of $\mu_{i,j}$ at $j = 1$ to solve the same equation at $j = 2$. According to Eq. (C5), $\mu_{i,j}$ at $j = 1$ and $j = 0$ can not be directly evaluated from $\phi_{i,j}$ with $i = 1, \dots, N_x$ and $j = 1, \dots, N_z$. But they can still be determined from the boundary conditions at $z = -L_z/2$. $\mu_{i,j}$ at $j = 0$ is obtained from $\partial_n \mu = 0$ at $j = 1$ as

$$\mu_{i,j-1=0} = \mu_{i,j+1=2}. \quad (\text{C9})$$

To obtain $\mu_{i,j}$ at $j = 1$, we need to determine $\phi_{i,j}$ at $j = 0$. This can be done by requiring that Eqs. (C1) and (C3) yield the same $\partial \phi / \partial t$ at $z = -L_z/2$. The discretized convection-diffusion equation is given by Eq. (C6) while the discretized relaxation equation for ϕ at the boundary $j = 1$ is given by

$$\frac{\partial}{\partial t} \phi_{i,j} + [\mathbf{v} \cdot \nabla \phi]_{i,j} = -\mathcal{V}_s \left[\frac{\phi_{i,j-1} - \phi_{i,j+1}}{2\Delta_z} - \frac{\sqrt{2}}{3} \cos \theta_s^0 s_\gamma(\phi_{i,j}) \right]. \quad (\text{C10})$$

Equating the right-hand side of Eq. (C6) at $j = 1$ (with $\mu_{i,0}$ fixed by Eq. (C9) and other μ 's given by Eq. (C5)) with that of Eq. (C10) leads to a tridiagonal system of linear equations for $\phi_{i,j}$ ($\phi_{i,j}$ coupled with $\phi_{i-1,j}$ and $\phi_{i+1,j}$) at $j = 0$. Solving this tridiagonal system determines $\phi_{i,j}$ at $j = 0$, from which we obtain $\mu_{i,j}$ at $j = 1$ by using Eq. (C5).

4. Navier-Stokes equation

We now turn to the Navier-Stokes equation (C2) with the incompressibility condition $\nabla \cdot \mathbf{v} = 0$. The difficulty in solving the Navier-Stokes equation is the lack of a time evolution equation for the pressure p . In the following, we will introduce a numerical method based on the pressure Poisson equation [23].

a. Pressure Poisson equation

Taking the divergence of momentum equation (C2) and applying the incompressibility condition, we obtain the pressure Poisson equation

$$\nabla^2 p = -\mathcal{R} \nabla \cdot [(\mathbf{v} \cdot \nabla) \mathbf{v}] + \mathcal{B} \nabla \cdot [(-\nabla^2 \phi - \phi + \phi^3) \nabla \phi]. \quad (\text{C11})$$

Dotting the momentum equation (C2) with the surface normal at the fluid-solid boundary and using $v_n = 0$, we obtain for Eq. (C11) the boundary condition

$$\partial_n p = \nabla^2 v_n + \mathcal{B}(-\nabla^2 \phi - \phi + \phi^3) \partial_n \phi, \quad (\text{C12})$$

at $z = \pm L_z/2$. In addition, we use $\nabla^2 p = 0$ and $\partial_x p = 0$ for the values of $\nabla^2 p$ and $\partial_n p$ at the boundaries $x = \pm L_x/2$. This reflects the single phase flow given by Eq. (C8).

From the momentum equation (C2) and the pressure Poisson equation (C11), we derive a diffusion equation

$$\mathcal{R} \frac{\partial(\nabla \cdot \mathbf{v})}{\partial t} = \nabla^2(\nabla \cdot \mathbf{v}),$$

for $\nabla \cdot \mathbf{v}$. With $\nabla \cdot \mathbf{v} = 0$ given at time $t = 0$, and in order to ensure that \mathbf{v} remains divergence-free at $t > 0$, we must impose the additional boundary condition $\nabla \cdot \mathbf{v} = 0$ at

all times $t \geq 0$. We will show that this boundary condition is needed in solving for p in a finite-difference scheme.

In order to solve the pressure Poisson equation, we need to evaluate $[\nabla^2 p]_{i,j}$ for $i = 1, \dots, N_x$ and $j = 1, \dots, N_z$, $[\partial_x p]_{i,j}$ for $i = 1, N_x$ and $j = 1, \dots, N_z$, and $[\partial_z p]_{i,j}$ for $i = 1, \dots, N_x$ and $j = 1, N_z$. For $\nabla^2 p$, we have

$$[\nabla^2 p]_{i,j} = 0,$$

for $i = 1, N_x$ and $j = 1, \dots, N_z$;

$$\begin{aligned} [\nabla^2 p]_{i,j} = & 2\mathcal{R} \left[\frac{v_{xi+1,j} - v_{xi-1,j}}{2\Delta_x} \frac{v_{zi,j+1} - v_{zi,j-1}}{2\Delta_z} - \frac{v_{zi+1,j} - v_{zi-1,j}}{2\Delta_x} \frac{v_{xi,j+1} - v_{xi,j-1}}{2\Delta_z} \right] \\ & + \mathcal{B} \mu_{i,j} \left(\frac{\phi_{i+1,j} - 2\phi_{i,j} + \phi_{i-1,j}}{\Delta_x^2} + \frac{\phi_{i,j+1} - 2\phi_{i,j} + \phi_{i,j-1}}{\Delta_z^2} \right) \\ & + \mathcal{B} \left(\frac{\mu_{i+1,j} - \mu_{i-1,j}}{2\Delta_x} \frac{\phi_{i+1,j} - \phi_{i-1,j}}{2\Delta_x} + \frac{\mu_{i,j+1} - \mu_{i,j-1}}{2\Delta_z} \frac{\phi_{i,j+1} - \phi_{i,j-1}}{2\Delta_z} \right), \end{aligned}$$

for $i = 2, \dots, N_x - 1$ and $j = 2, \dots, N_z - 1$; and

$$\begin{aligned} [\nabla^2 p]_{i,j} = & 2\mathcal{R} \frac{v_{xi+1,j} - v_{xi-1,j}}{2\Delta_x} \frac{v_{zi,j+1} - v_{zi,j-1}}{2\Delta_z} \\ & + \mathcal{B} \mu_{i,j} \left(\frac{\phi_{i+1,j} - 2\phi_{i,j} + \phi_{i-1,j}}{\Delta_x^2} + \frac{\phi_{i,j+1} - 2\phi_{i,j} + \phi_{i,j-1}}{\Delta_z^2} \right) \\ & + \mathcal{B} \frac{\mu_{i+1,j} - \mu_{i-1,j}}{2\Delta_x} \frac{\phi_{i+1,j} - \phi_{i-1,j}}{2\Delta_x}, \end{aligned}$$

for $i = 2, \dots, N_x - 1$ and $j = 1, N_z$ (where $v_z = 0$ and $\partial_z \mu = 0$). We see that ϕ and v_z at ghost sites of $j = 0, N_z + 1$ appear in the last expression. The ghost ϕ 's have already been determined in solving the convection-diffusion equation, while the ghost v_z 's are determined through the additional boundary condition $\nabla \cdot \mathbf{v} = 0$:

$$\frac{v_{xi+1,j} - v_{xi-1,j}}{2\Delta_x} + \frac{v_{zi,j+1} - v_{zi,j-1}}{2\Delta_z} = 0,$$

for $i = 2, \dots, N_x - 1$, and $j = 1, N_z$. For $\partial_n p$, we have

$$[\partial_x p]_{i,j} = 0$$

for $i = 1, N_x$ and $j = 1, \dots, N_z$;

$$[\partial_z p]_{i,j} = 0$$

for $i = 1, N_x$ and $j = 1, N_z$; and

$$[\partial_z p]_{i,j} = \frac{v_{zi,j+1} + v_{zi,j-1}}{\Delta_z^2} + \mathcal{B}\mu_{i,j} \frac{\phi_{i,j+1} - \phi_{i,j-1}}{2\Delta_z}$$

for $i = 2, \dots, N_x - 1$ and $j = 1, N_z$ (where $v_z = 0$). The last expression involves the ghost ϕ 's and v_z 's at $j = 0, N_z + 1$. Given the above values of $[\nabla^2 p]_{i,j}$ and $[\partial_n p]_{i,j}$, we apply a 2D Fast Fourier Transformation to solve $p_{i,j}(0)$ (up to a constant) for $i = 1, \dots, N_x$ and $j = 1, \dots, N_z$.

b. Slip boundary condition

The discretized Navier-Stokes equation is given by

$$\begin{aligned} \frac{\partial v_{xi,j}}{\partial t} = & -v_{xi,j} \frac{v_{xi+1,j} - v_{xi-1,j}}{2\Delta_x} - v_{zi,j} \frac{v_{xi,j+1} - v_{xi,j-1}}{2\Delta_z} - \frac{1}{\mathcal{R}} \frac{p_{i+1,j} - p_{i-1,j}}{2\Delta_x} \\ & + \frac{1}{\mathcal{R}} \left(\frac{v_{xi+1,j} - 2v_{xi,j} + v_{xi-1,j}}{\Delta_x^2} + \frac{v_{xi,j+1} - 2v_{xi,j} + v_{xi,j-1}}{\Delta_z^2} \right) \\ & + \frac{\mathcal{B}}{\mathcal{R}} \mu_{i,j} \frac{\phi_{i+1,j} - \phi_{i-1,j}}{2\Delta_x}, \end{aligned} \quad (\text{C13})$$

for $i = 2, \dots, N_x - 1$ and $j = 1, \dots, N_z$, and

$$\begin{aligned} \frac{\partial v_{zi,j}}{\partial t} = & -v_{xi,j} \frac{v_{zi+1,j} - v_{zi-1,j}}{2\Delta_x} - v_{zi,j} \frac{v_{zi,j+1} - v_{zi,j-1}}{2\Delta_z} - \frac{1}{\mathcal{R}} \frac{p_{i,j+1} - p_{i,j-1}}{2\Delta_z} \\ & + \frac{1}{\mathcal{R}} \left(\frac{v_{zi+1,j} - 2v_{zi,j} + v_{zi-1,j}}{\Delta_x^2} + \frac{v_{zi,j+1} - 2v_{zi,j} + v_{zi,j-1}}{\Delta_z^2} \right) \\ & + \frac{\mathcal{B}}{\mathcal{R}} \mu_{i,j} \frac{\phi_{i,j+1} - \phi_{i,j-1}}{2\Delta_z}. \end{aligned} \quad (\text{C14})$$

for $i = 2, \dots, N_x - 1$ and $j = 2, \dots, N_z - 1$, together with the boundary conditions that $v_{zi,j} = 0$ at $j = 1, N_z$ and \mathbf{v} given by Eq. (C8) at $i = 1, N_x$. Equation (C13) at $j = 1, N_z$ involves ϕ and v_x at ghost sites of $j = 0, N_z + 1$. The ghost ϕ 's come from $\mu_{i,j}$ at $j = 1, N_z$, and have already been determined. The ghost v_x 's are determined from the discretized GNBC

$$[\mathcal{L}_s(\phi_{i,j})]^{-1} v_{xi,j}^{slip} = \mathcal{B} \left[\frac{\phi_{i,j-1} - \phi_{i,j+1}}{2\Delta_z} - \frac{\sqrt{2}}{3} \cos \theta_s^0 s_\gamma(\phi_{i,j}) \right] \frac{\phi_{i+1,j} - \phi_{i-1,j}}{2\Delta_x} - \frac{v_{xi,j-1} - v_{xi,j+1}}{2\Delta_z}, \quad (\text{C15})$$

at the lower boundary $j = 1$ with $v_{xi,j}^{slip} = v_{xi,j} - V$, and

$$[\mathcal{L}_s(\phi_{i,j})]^{-1} v_{xi,j}^{slip} = \mathcal{B} \left[\frac{\phi_{i,j+1} - \phi_{i,j-1}}{2\Delta_z} - \frac{\sqrt{2}}{3} \cos \theta_s^0 s_\gamma(\phi_{i,j}) \right] \frac{\phi_{i+1,j} - \phi_{i-1,j}}{2\Delta_x} - \frac{v_{xi,j+1} - v_{xi,j-1}}{2\Delta_z}, \quad (\text{C16})$$

at the upper boundary $j = N_z$ with $v_{xi,j}^{slip} = v_{xi,j} + V$.

In summary, to solve the dynamic equations (9) and (10), we need to use $\phi = \pm 1$ and Eq. (C8) at $x = \pm L_x/2$, with $v_n = 0$, $\partial_n \mu = 0$, plus Eqs. (14) and (15) at $z = \pm L_z/2$. In particular, in applying the boundary conditions at $z = \pm L_z/2$, values of ϕ , v_x , and v_z at ghost sites have to be introduced and solved for.

5. Time integration

We outline the scheme for time discretization and integration. For simplicity we only describe the forward Euler time stepping. In the following a superscript n denotes consecutive time instants and Δt is the time interval.

Time Stepping: Given $\{\phi_{i,j}^n\}$ and $\{\mathbf{v}_{i,j}^n\}$ at all the sites ($i = 1, \dots, N_x$ and $j = 1, \dots, N_z$) in the system:

Step 1: Determine $\{\mu_{i,j}^n\}$, $\{\phi_{i,j}^n\}$, and $\{\mathbf{v}_{i,j}^n\}$ at the ghost sites from the various boundary conditions, as described in Secs. C 3, C 4 a, and C 4 b.

Step 2: Solve $\{p_{i,j}^n\}$ at all the interior sites ($i = 1, \dots, N_x$ and $j = 1, \dots, N_z$) from Eq. (C11) with appropriate boundary conditions for $\partial_n p$, as described in Sec. C 4 a.

Step 3: Compute $\{\phi_{i,j}^{n+1}\}$ and $\{\mathbf{v}_{i,j}^{n+1}\}$ at all the interior sites (except those fixed by the boundary conditions at all times) using

$$\frac{\phi^{n+1} - \phi^n}{\Delta t} = -\mathbf{v}^n \cdot \nabla \phi^n + \mathcal{L}_d \nabla^2 \mu^n,$$

and

$$\mathcal{R} \frac{\mathbf{v}^{n+1} - \mathbf{v}^n}{\Delta t} = -\mathcal{R} (\mathbf{v}^n \cdot \nabla) \mathbf{v}^n - \nabla p^n + \nabla^2 \mathbf{v}^n + \mathcal{B} \mu^n \nabla \phi^n,$$

according to Eqs. (C6), (C13), and (C14) in discretized time. Here the ghost $\{\mu_{i,j}^n\}$, $\{\phi_{i,j}^n\}$, and $\{\mathbf{v}_{i,j}^n\}$ determined in Step 1 and $\{p_{i,j}^n\}$ solved in Step 2 are needed.

REFERENCES

- [1] C. Huh and S. G. Mason, *J. Fluid Mech.* **81**, 401 (1977).
- [2] E. B. Dussan, V., *Ann. Rev. Fluid Mech.* **11**, 371 (1979).
- [3] J. F. Joanny and P. G. de Gennes, *J. Chem. Phys.* **81**, 552 (1984).
- [4] P. G. de Gennes, *Rev. Mod. Phys.* **57**, 827 (1985).
- [5] R. G. Cox, *J. Fluid. Mech.* **168**, 169 (1986).
- [6] J. Koplik, J. R. Banavar, and J. F. Willemsen, *Phys. Rev. Lett.* **60**, 1282 (1988); J. Koplik, J. R. Banavar, and J. F. Willemsen, *Phys. Fluids A* **1**, 781 (1989).
- [7] P. A. Thompson and M. O. Robbins, *Phys. Rev. Lett.* **63**, 766 (1989); P. A. Thompson, W. B. Brinckerhoff, and M. O. Robbins, *J. Adhesion Sci. Tech.* **7**, 535 (1993).
- [8] M. Y. Zhou and P. Sheng, *Phys. Rev. Lett.* **64**, 882 (1990).
- [9] G. J. Merchant and J. B. Keller, *Phys. Fluids A* **4**, 477 (1992).
- [10] Blake first proposed that the uncompensated Young stress contributes to the relative slipping, in the context of an adsorption/desorption model. See T. D. Blake, *Dynamic contact angles and wetting kinetics*, in *Wettability*, edited by J. C. Berg (Marcel Dekker, Inc., 1993) p.251.
- [11] H. Y. Chen, D. Jasnow, and J. Vinals, *Phys. Rev. Lett.* **85**, 1686 (2000).
- [12] D. Jacqmin, *J. Fluid. Mech.* **402**, 57 (2000).
- [13] P. A. Thompson and S. M. Troian, *Nature* **389**, 360 (1997).
- [14] M. Allen and D. Tildesley, *Computer Simulation of Liquids* (Clarendon, New York, 1987).
- [15] For the contribution of intermolecular forces to the stress, we have directly measured the fluid-fluid interaction forces across bin surfaces instead of using the Irving-Kirkwood

expression (J. H. Irving and J. G. Kirkwood, J. Chem. Phys. **18**, 817 (1950)), whose validity was noted to be not justified at the fluid-fluid or the wall-fluid interface (see the paragraph following equation (5.15) in the above reference).

- [16] Inertial effect was found to be less than σ_{nx} by two orders of magnitude.
- [17] This relation is obtained by assuming the two fluids interacting independently with the wall, so that \tilde{G}_x^f may be expressed as the weighted average of $\tilde{G}_x^{f1} = \beta_1 v_x^{slip1}$ and $\tilde{G}_x^{f2} = \beta_2 v_x^{slip2}$. The desired expression is obtained by noting $v_x^{slip1} \simeq v_x^{slip2}$ to within 10%.
- [18] According to the mechanical definition of interfacial tension, γ equals to the integral (across the interface) of the difference between the normal and parallel components of the pressure, $\gamma = \int dl [P_\perp(l) - P_\parallel(l)]$, where l is along the interface normal, and P_\perp and P_\parallel are the pressure-tensor components normal and parallel to the interface, respectively (far from the interface $P_\perp = P_\parallel$). See J. G. Kirkwood and F. P. Buff, J. Chem. Phys. **17**, 338 (1949). The Laplace's equation, plus the fact that $-\int_{\text{int}} dx \sigma_{nx}^Y(z) = \gamma \cos \theta_d(z)$ and $-\int_{\text{int}} dx \sigma_{nx}^0(z) = \gamma \cos \theta_s(z)$ for curved (fluid-fluid) interfaces, can be derived from the above expression for γ , together with force balance considerations. Our MD simulation results thus confirm this definition of the surface tension.
- [19] J. W. Cahn and J. E. Hilliard, J. Chem. Phys. **28**, 258 (1958).
- [20] From MD simulations, the interface $\xi \simeq 0.3\sigma$, with a profile very accurately described by the $\tanh(x/\sqrt{2}\xi)$ form predicted by the CH free energy. The small value of ξ implies negligible diffusion across the interface.
- [21] L. D. Landau and E. M. Lifshitz, *Fluid Mechanics* (Butterworth-Heinemann, Oxford, 1998).
- [22] For gently curved interfaces, $\int_{\text{int}} dx [K \partial_n \phi \partial_x \phi] = \int_{\text{int}} d\phi (K \partial_l \phi) \cos \theta_d^0$, where ∂_l means taking partial derivative with respect to (fluid-fluid) interface normal l , with $\partial_n \phi$ approx-

imated by $\partial_l \phi \cos \theta_d^0$. As $\int_{\text{int}} d\phi (K \partial_l \phi) = \int_{\text{int}} dl K (\partial_l \phi)^2 = \gamma$, we have $\int_{\text{int}} dx [K \partial_n \phi \partial_x \phi] = \gamma \cos \theta_d^0$.

- [23] H. Johnston and J. G. Liu, *J. Comput. Phys.* **180**, 120 (2002).
- [24] Weinan E, *Numerical methods for viscous incompressible flow: Some recent advances*, in *Advances in scientific computing* (Science Press, 2001) p.29.
- [25] Agreement between continuum hydrodynamics and MD simulation has been demonstrated by treating the slip profile (v_x^{slip} along the wall, derived from MD simulations) and the dynamic contact angle as inputs to the continuum model, see N. G. Hadji-costantinou, *Phys. Rev. E* **59**, 2475 (1999). The significance of our results lies in the fact that no such information have been put in by hand.
- [26] The breakup of the interface (with a film left behind the moving CL) has been observed for both the Couette and Poiseuille flows at large Ca [6,7].
- [27] Nanometer-scale details may be resolved through the grid iteration method without significantly compromising the computation efficiency. See W. Ren and X. P. Wang, *J. Comput. Phys.* **159**, 246 (2000).
- [28] M. Cieplak, J. Koplik, and J. R. Banavar, *Phys. Rev. Lett.* **86**, 803 (2001).
- [29] J-x. Yang, J. Koplik, and J. R. Banavar, *Phys. Rev. Lett.* **67**, 3539 (1991); J-L. Barrat and L. Bocquet, *Phys. Rev. Lett.* **82**, 4671 (1999).

FIGURES

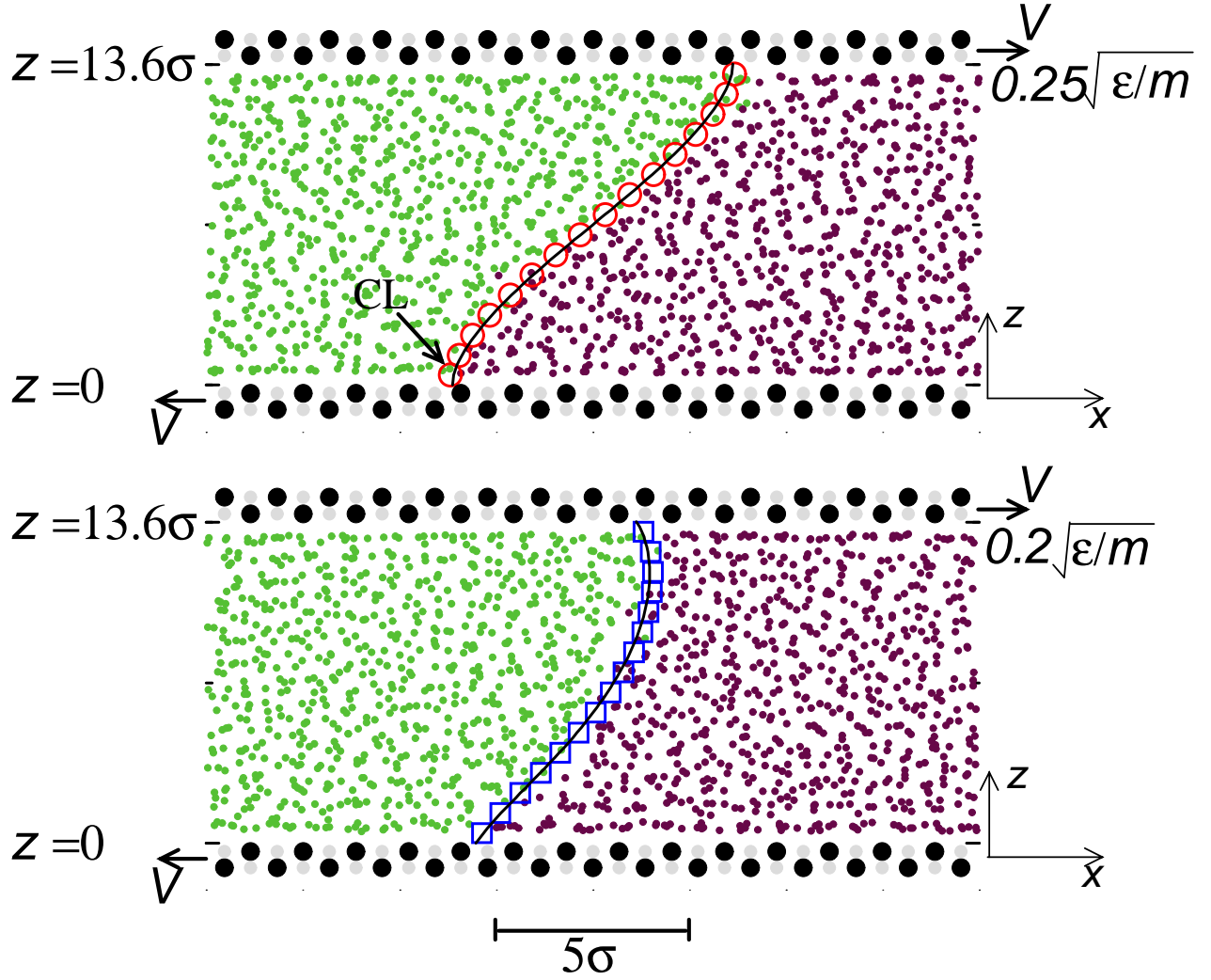


FIG. 1. Segments of the MD simulation sample for the immiscible Couette flows. The colored dots indicate the instantaneous molecular positions of the two fluids projected onto the xz plane. The black/gray circles denote the wall molecules. The upper panel illustrates the symmetric case; the lower panel illustrates the asymmetric case. The red circles and the blue squares represent the time-averaged interface profiles, defined by $\rho_1 = \rho_2$ ($\phi = 0$), for the two cases. The black solid lines are the interface profiles calculated from the continuum hydrodynamic model with the GNBC.

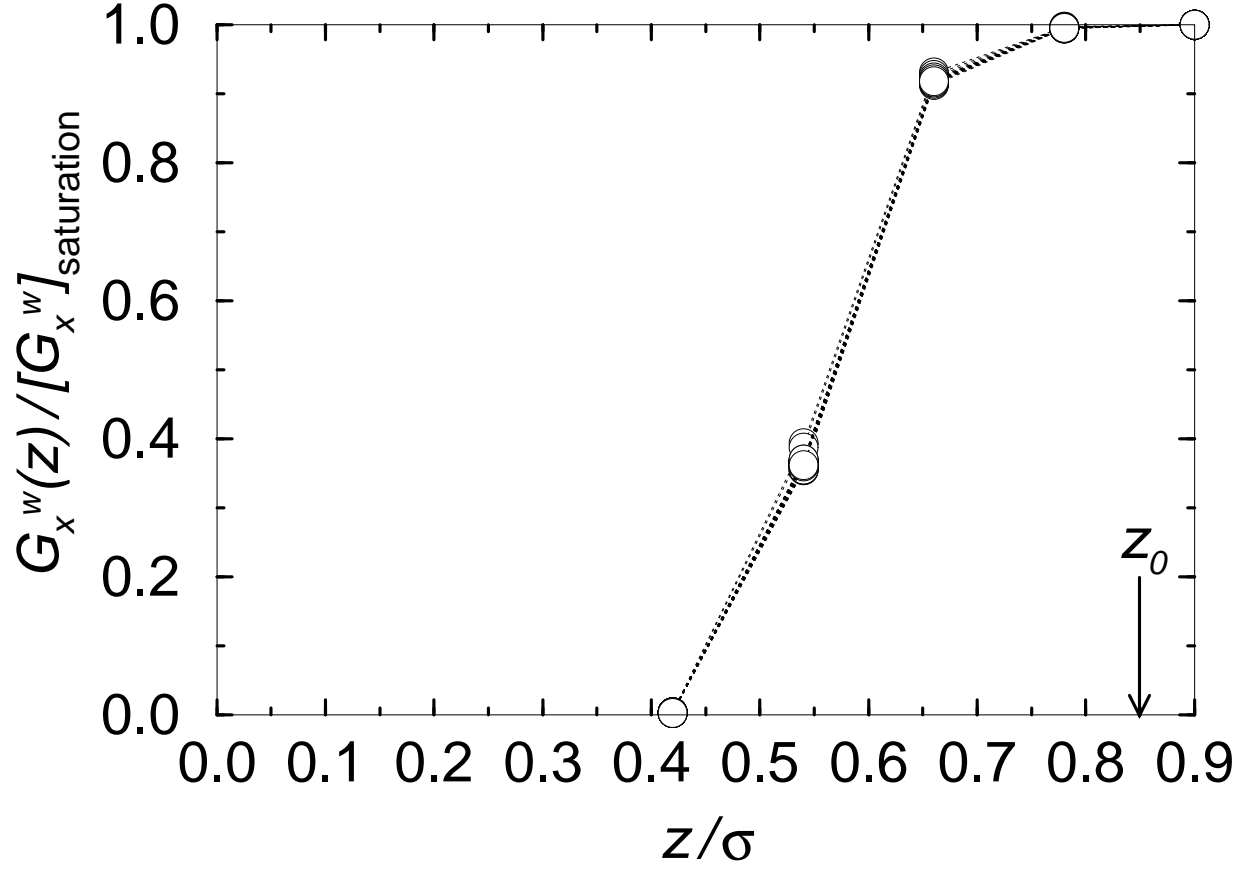


FIG. 2. By subdividing the boundary layer into thin sections, we plot the measured total wall force per unit wall area as a function of distance z away from the boundary. For different x positions, the absolute value of the saturating total wall force is different. However, when normalized by the corresponding saturated total wall force per unit area at each x , all points fall on a universal curve, independent of x . It is seen that at $z = z_0$ the wall force has reached its saturation value.

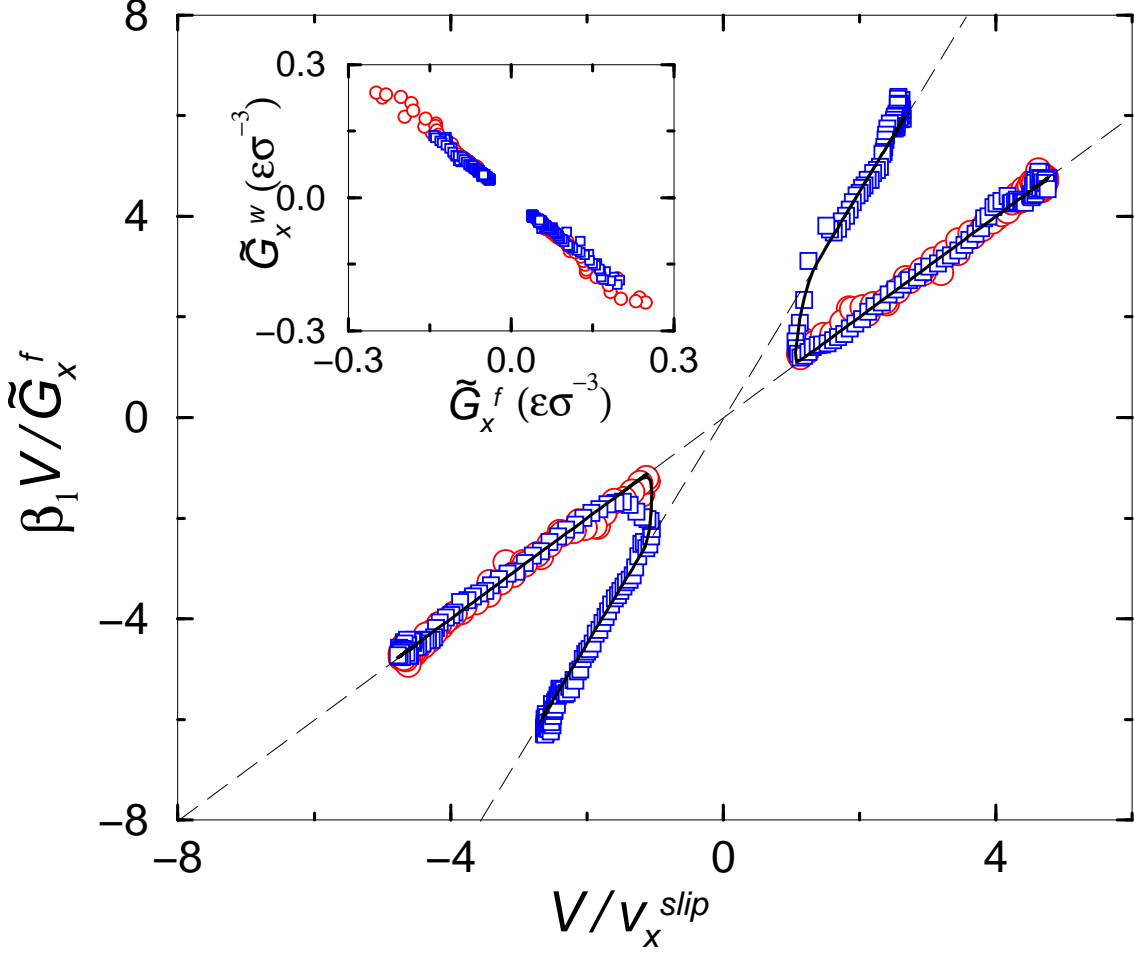


FIG. 3. $\beta_1 V / \tilde{G}_x^f$ plotted as a function of V / v_x^{slip} . Symbols are MD data measured in the BL at different x locations, where the red circles denote the symmetric case and the blue squares the asymmetric case. The solid lines were calculated from Eq. (1) with values of $\beta_{1,2}$ and the expression of β given in the text. The statistical errors of the MD data are about the size of the symbols. The upper-right data segment corresponds to the lower boundary, whereas the lower-left segment corresponds to the upper boundary. The slopes of the two dashed lines are given by $\beta_{1,2}^{-1}$. Inset: \tilde{G}_x^w plotted as a function of \tilde{G}_x^f , measured in the two BL's at different values of x . The symbols have the same correspondence as in the main figure. The data are seen to lie on a straight line with a slope of -1 , indicating $\tilde{G}_x^w + \tilde{G}_x^f = 0$.

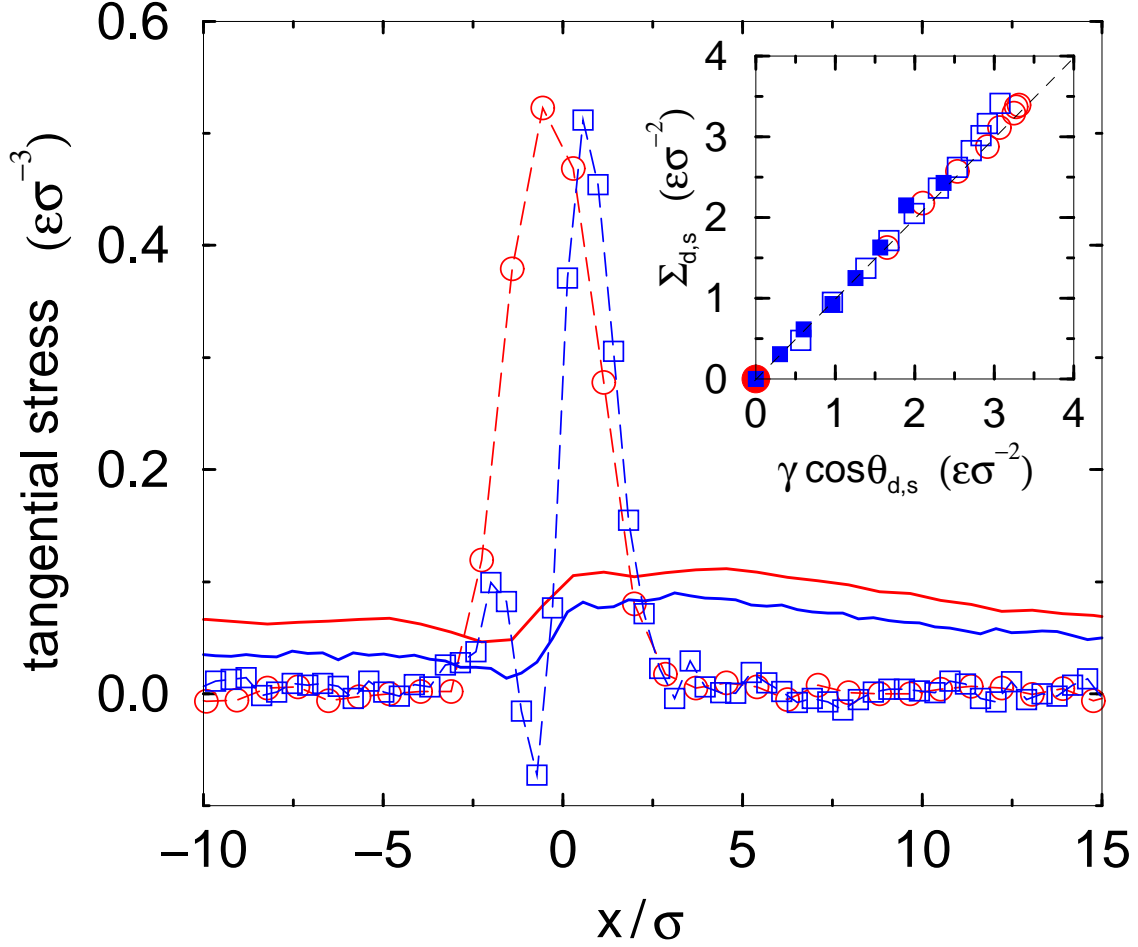


FIG. 4. Two components of the dynamic tangential stress at $z = z_0$, plotted as a function of x . The dashed lines denote $\tilde{\sigma}_{zx}^Y$; solid lines represent the viscous component. Here red indicates the symmetric case and blue the asymmetric case. In the CL region the non-viscous component is one order of magnitude larger than the viscous component. The difference between the two components, however, diminishes towards the boundary, $z = 0$, due to the large interfacial pressure drop (implying a large curvature) in the BL, thereby pulling θ_d closer to θ_s . Inset: $\Sigma_{d,s}$ plotted as a function of $\gamma \cos \theta_{d,s}$ at different values of z . Here $\Sigma_d = -\int dx(\sigma_{nx} - \sigma_{nx}^v)$, $\Sigma_s = -\int dx \sigma_{nx}^0$, and $\theta_{d,s}$ was measured from the time-averaged interfacial profiles (Fig. 1). The red circles denote the symmetric case, the blue squares the asymmetric case, the solid blue squares the asymmetric static case, and the single solid red circle at the origin denotes the symmetric static case. The data are seen to follow a straight (dashed) line with slope 1, indicating $\Sigma_{d,s} = \gamma \cos \theta_{d,s}$.

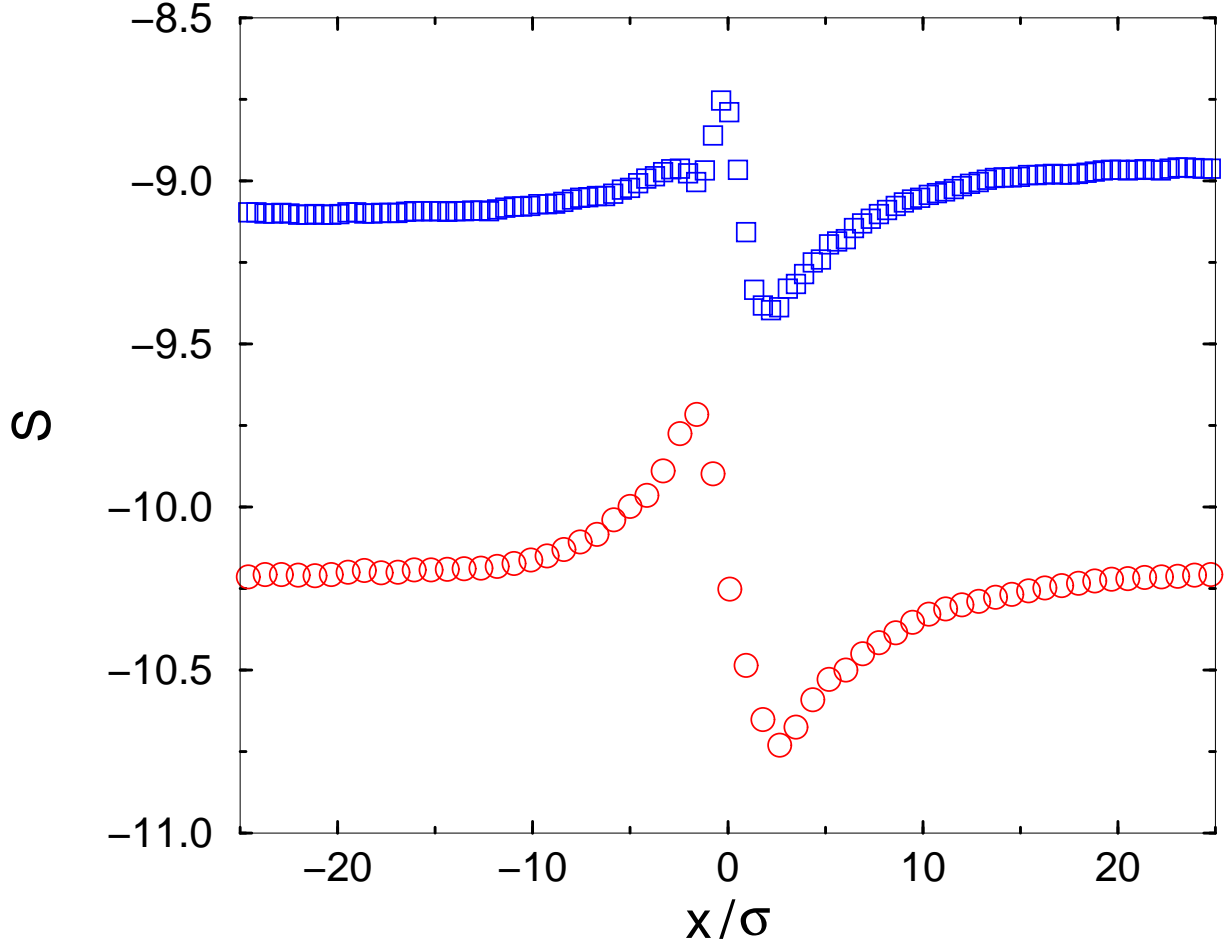


FIG. 5. $S = \int_0^{z_0} \tilde{\sigma}_{xx}(z) dz$ plotted as a function of x . Here red circles denote the symmetric case and blue squares the asymmetric case.

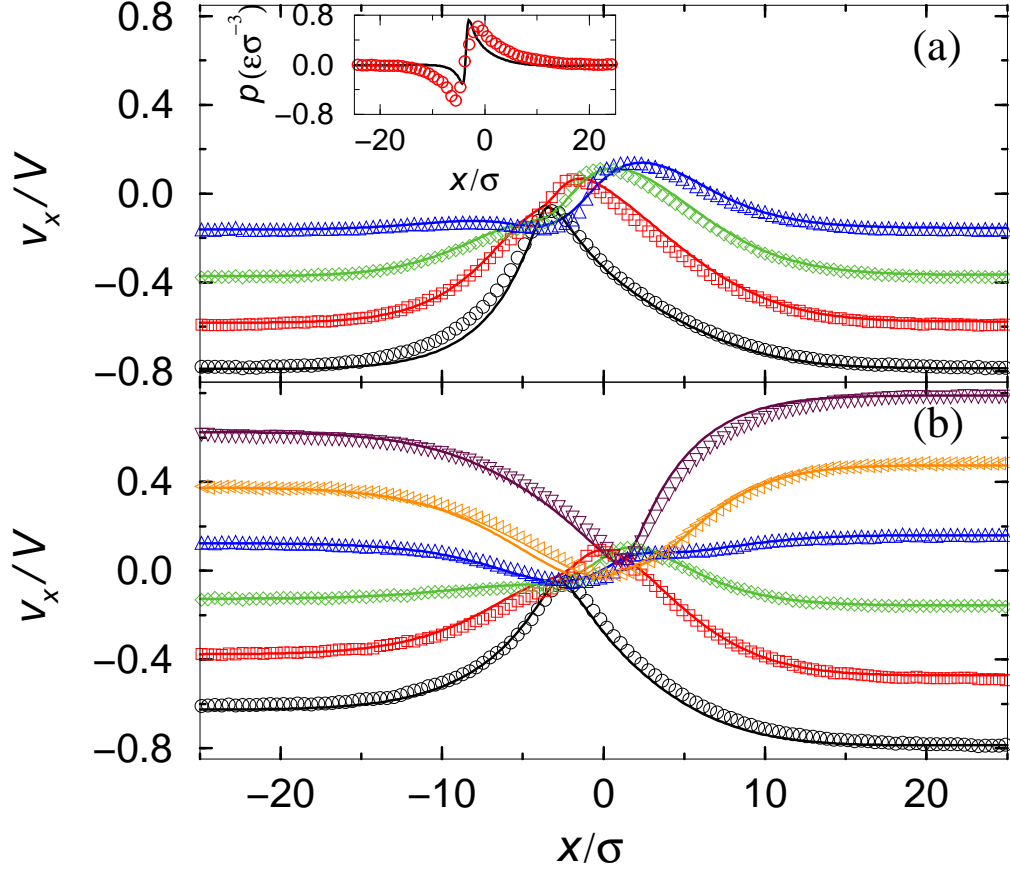


FIG. 6. Comparisons between the MD (symbols) and the continuum hydrodynamics (solid lines) results for the Couette flow, the latter calculated with the GNBC and values of $M = 0.023\sigma^4/\sqrt{m\epsilon}$ and $\Gamma = 0.66\sigma/\sqrt{m\epsilon}$. (a) The v_x profiles for the symmetric case ($V = 0.25(\epsilon/m)^{1/2}$ and $H = 13.6\sigma$) at different z planes. The profiles are symmetric about the center plane, hence only the lower half is shown for $z = 0.425\sigma$ (black circles), 2.125σ (red squares), 3.825σ (green diamonds), and 5.525σ (blue triangles). (b) The v_x profiles for the asymmetric case ($V = 0.2(\epsilon/m)^{1/2}$ and $H = 13.6\sigma$) at $z = 0.425\sigma$ (black circles), 2.975σ (red squares), 5.525σ (green diamonds), 8.075σ (blue triangles), 10.625σ (yellow triangles), 13.175σ (maroon triangles). For the boundary layers, $v_x = 0$ means complete slip. Inset: Pressure variation in the BL for the symmetric case. The solid line represents the BL-averaged hydrodynamic pressure $z_0^{-1} \int_0^{z_0} p(z) dz$ from the continuum model, and red circles denote $z_0^{-1} \int_0^{z_0} \tilde{\sigma}_{xx}(z) dz$ measured in MD simulations (see Fig. 5). Note the fast variation across the interface. The interfacial pressure drop in the BL is a factor 5 – 10 larger than that in the middle of the sample, implying large curvature.

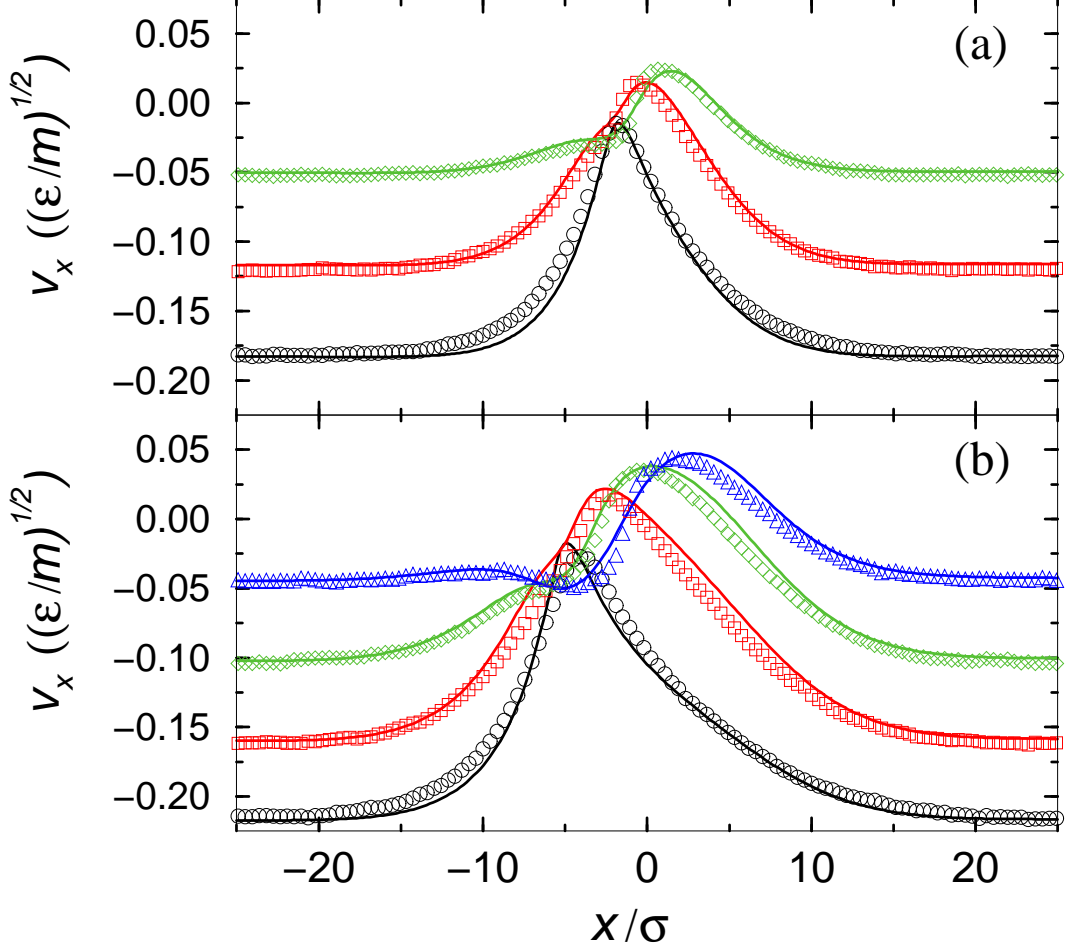


FIG. 7. Comparisons between the MD (symbols) and the continuum hydrodynamics (solid lines) results for two symmetric cases in the Couette flow geometry. Compared with Fig. 6a, V and H have been varied, respectively, but the continuum results are calculated with the same set of parameters and the GNBC. The profiles are symmetric about the center plane, hence only the lower half is shown. (a) The v_x profiles for $V = 0.25(\epsilon/m)^{1/2}$ and $H = 10.2\sigma$, shown at $z = 0.425\sigma$ (black circles), 2.125σ (red squares), and 3.825σ (green diamonds). (b) The v_x profiles for $V = 0.275(\epsilon/m)^{1/2}$ and $H = 13.6\sigma$, shown at $z = 0.425\sigma$ (black circles), 2.125σ (red squares), 3.825σ (green diamonds), and 5.525σ (blue triangles).

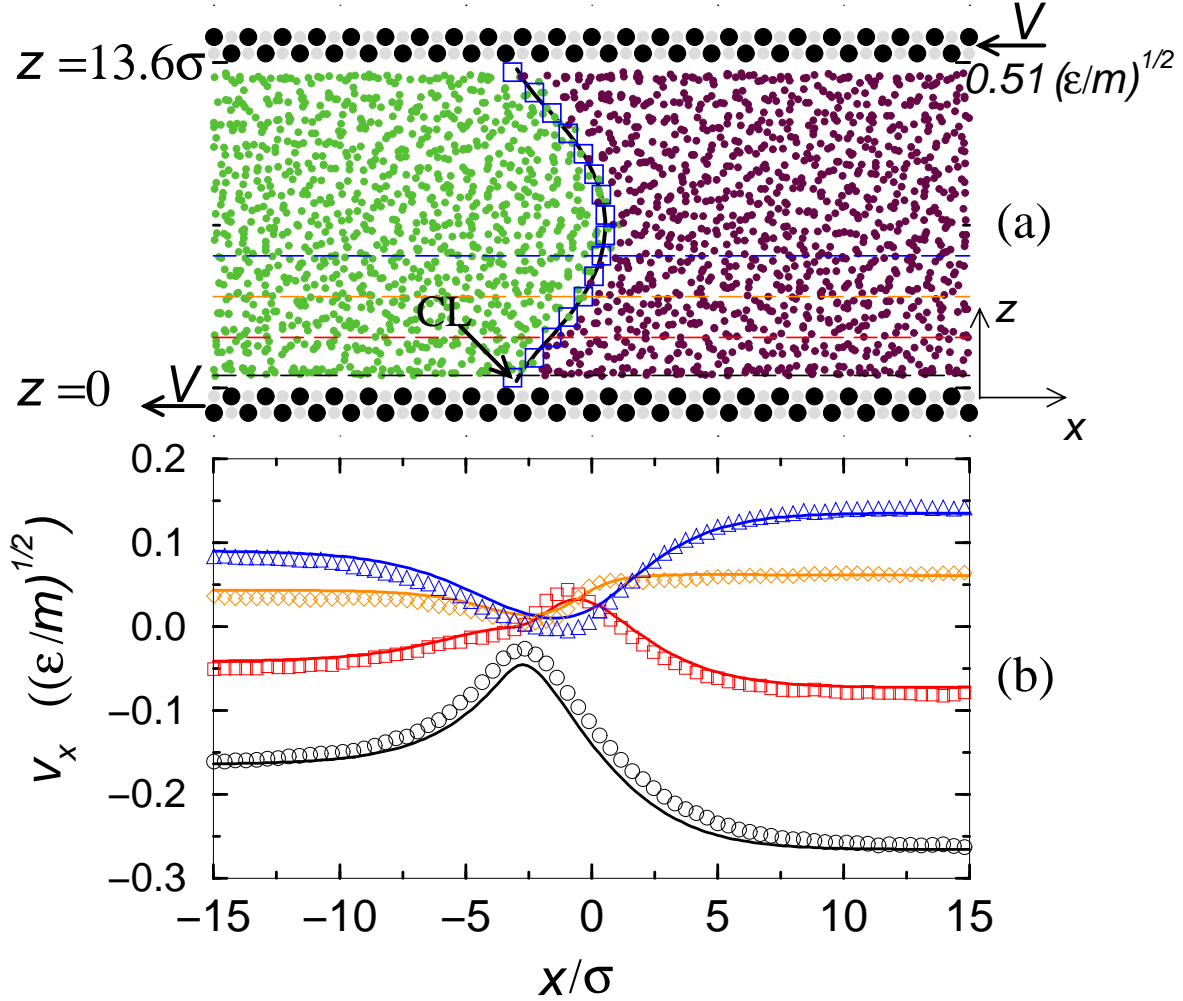


FIG. 8. Comparisons between the MD (symbols) and the continuum hydrodynamics (solid lines) results for an asymmetric case in the Poiseuille flow geometry. Compared with Fig. 6b, the type of flow has been changed, but the continuum results are calculated with the same set of parameters. (a) A segment of the instantaneous configuration in the MD simulation. The two walls, separated by $H = 13.6\sigma$, move at a constant speed $V = 0.51(\epsilon/m)^{1/2}$ in the $-x$ direction in order to maintain a time-independent steady-state interface, with $mg_{ext} = 0.05\epsilon/\sigma$ applied in the x direction. The symbols have the same correspondence as those in Fig. 1b. The black solid line is the interface profiles calculated from the continuum hydrodynamic model. The colored dashed lines indicate the z coordinates of the v_x profiles shown in (b). (b) The v_x profiles at $z = 0.425\sigma$ (black circles), 2.125σ (red squares), 3.825σ (green diamonds), and 5.525σ (blue triangles). The profiles are symmetric about the center plane, hence only the lower half is shown.

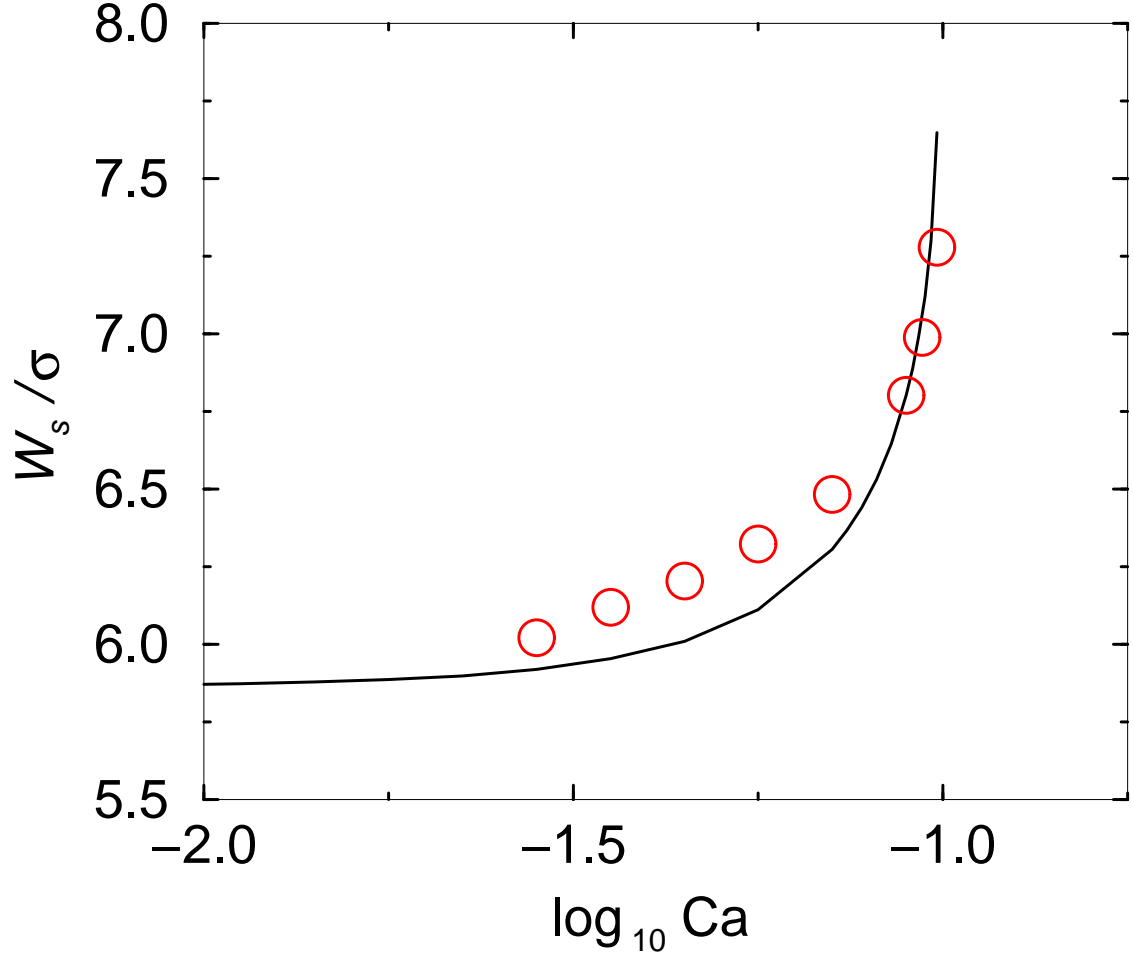


FIG. 9. Width for the moving CL region, W_s , plotted as a function of the capillary number $Ca = \eta V / \gamma$ for the symmetric case by varying V and keeping $H = 13.6\sigma$. We note that for most of the MD data measured in the symmetric case, $Ca \simeq 0.088$. Solid line was calculated from the immiscible hydrodynamic model employing the GNBC; red circles denote the MD results.

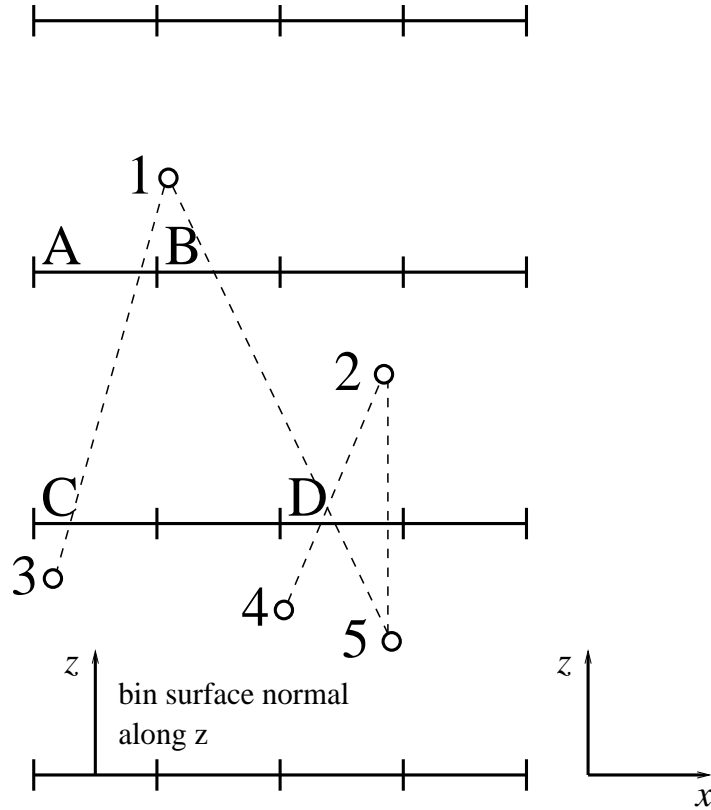


FIG. 10. Schematic illustration of measuring the zx component of σ_U . The horizontal solid lines (separated by short vertical lines) represent bin surfaces with surface normals along the z direction. Circles denote fluid molecules. The dashed lines connect pairs of interacting molecules. Here the bin surfaces and the molecules are projected onto the xz plane. Molecules that appear to be close to each other may not be in the interaction range if their distance along y is too large. A pair of interacting molecules may act across more than one bin surface. Here the (1,3) pair acts across the surfaces A and C while the (1,5) pair acts across the surfaces B and D. At each bin surface the stress measurement must run over all the pairs that act across that surface. For surface D, there are three pairs of interacting molecules (1,5), (2,4), and (2,5) that contribute to the zx component of σ_U .